

THE PROPERTIES OF THE MID- TO FAR-INFRARED EMISSION IN THE LARGE MAGELLANIC CLOUD

ITSUKI SAKON,¹ TAKASHI ONAKA,¹ HIDEHIRO KANEDA,² DAISUKE TOKURA,¹ TOSHINOBU TAKAGI,² YUKA Y. TAJIRI,^{1,3}
 HIDENORI TAKAHASHI,¹ DAISUKE KATO,⁴ TOSHIKAZU ONISHI,⁴ AKIKO KAWAMURA,⁴ AND YASUO FUKUI⁴

Received 2006 April 17; accepted 2006 July 6

ABSTRACT

We investigate the properties of mid- to far-infrared emission in the Large Magellanic Cloud (LMC) based on the *COBE* DIRBE and *IRAS* Sky Survey Atlas data sets. We focus on the properties of far-infrared (FIR) thermal emission carried by submicron dust and mid-infrared (MIR) excess emission by very small grains in the LMC in comparison to those in the Milky Way. We carefully estimate the dust temperature by decomposing the various structures including young star clusters, supergiant shells, and CO molecular clouds and examine the MIR to FIR spectral energy distribution (SED) associated with each structure in the LMC. The amount of the MIR excess emission in 12 and 25 μm relative to the total FIR emission (F_{FIR}) in the LMC is generally smaller than that in the Milky Way, which confirms the scarcity of very small grains suggested by past studies on the extinction curve. The characteristics of 25 and 60 μm excess emission proportional to the square of the incident radiation field strength appear around young star clusters in the LMC. This sequence can be reproduced by the superposition of dust emission under different radiation field strengths ranging from 1 to 10^5 times of that in the solar vicinity. Finally, the MIR to FIR SEDs in CO molecular clouds in the LMC are discussed. Through these attempts, we succeed in completely explaining the characteristics of mid- to far-infrared SEDs given by the infrared broadband photometric data sets in terms of the superposition of the standard stochastic heating dust model.

Subject headings: dust, extinction — infrared: galaxies — Magellanic Clouds

1. INTRODUCTION

Infrared emission from diffuse interstellar dust consists of the unidentified infrared (UIR) bands as well as the far-infrared (FIR) emission dominated by the thermal emission from big ($\simeq 0.1 \mu\text{m}$) grains (BGs) in radiative equilibrium. In addition, there is excess emission at 25–60 μm , which is supposed to be carried by very small ($\simeq 10 \text{ nm}$) grains (VSGs) stochastically heated by absorbing a single ultraviolet (UV) photon and releasing the energy in the mid-infrared (MIR; Draine & Anderson 1985). However, quite little is known about the properties of this MIR excess emission. Several attempts have been performed to characterize it. The proportionality of the UIR intensity of the 7.7 μm band as well as the 6.2 and 11.2 μm bands to the integrated incident radiation intensity U over a wide range of $U = 1$ –100 in units of the incident radiation intensity in the solar vicinity was reported by Onaka (2000) based on the spectroscopic data sets obtained by the Mid-Infrared Spectrometer (MIRS) on board the *Infrared Telescope in Space* (IRTS). On the other hand, different behavior in the 25–60 μm excess emission, such that it seems to be roughly proportional to U^2 , was indicated (Onaka 2000). Further analysis of the MIR excess emission relative to the FIR emission in the diffuse Galactic radiation has revealed bipolar sequences in the color of the Diffuse Infrared Background Experiment (DIRBE) 60–100 μm intensity $f(60)/f(100)$ against the dust equilibrium temperature T_d of BGs (Sakon et al. 2004). They have found that the data for $|b| < 1.2$ form a steeply increasing sequence of

$f(60)/f(100)$ against T_d (sequence A), while those for $|b| > 1.2$ form a rather flat sequence of $f(60)/f(100)$ against T_d (sequence B). In the Galactic plane, we observe the interstellar dust emission from various objects superposed on the line of sight, and the interstellar extinction varies from direction to direction with Galactic longitude. It is thus difficult to specify the physical conditions at the position where the observed emission originates and to elucidate the mechanism that produces such bipolar sequences. Any precise interpretation of the spectral energy distribution (SED) variations revealed by the *Infrared Astronomical Satellite* (IRAS) or *Cosmic Background Explorer* (COBE) observations has not been made as successfully as for the diffuse interstellar emission. It is crucial to investigate how the variations in the physical conditions act on the infrared SED. For this purpose, observations of nearby targets in which various astrophysical environments can be decomposed would be quite effective. The Large Magellanic Cloud (LMC) has so far been one of the most attractive targets for investigating the nature of interstellar dust under various physical conditions owing to its nearby location at a distance of 50 kpc and its nearly face-on geometry. In the LMC we can resolve $\simeq 50 \text{ pc}$ scale structures with the *IRAS* data set, including young star clusters, giant molecular clouds, star-forming regions, and supergiant shells, without confusing them with one another.

Several studies based on the analysis of the extinction curves have given insight into the properties of interstellar dust in the LMC. The extinction curve of the LMC was first reported by Nandy et al. (1979), and significant differences in their spectra between in the LMC and in the Milky Way were indicated. The extinction curve in the LMC showed a weaker 2175 Å bump with a steeper far-ultraviolet (FUV) rise than that in the Milky Way. Recent studies have reported the variety of the extinction characteristics within the LMC; e.g., the 2175 Å bump inside the supergiant shell LMC 2 is weaker than that outside the shell (Misselt et al. 1999; Cartledge et al. 2005). Weingartner & Draine (2001)

¹ Department of Astronomy, School of Science, University of Tokyo, 7-3-1 Hongo, Bunkyo-ku, Tokyo 113-0033, Japan; isakon@astron.s.u-tokyo.ac.jp.

² Institute of Space and Astronautical Science, Japan Aerospace Exploration Agency, 3-1-1 Yoshinodai, Sagami-hara, Kanagawa 229-8510, Japan.

³ Department of Astronomy, Faculty of Science, Kyoto University, Sakyo-ku, Kyoto 606-8502, Japan.

⁴ Department of Astrophysics, Nagoya University, Chikusa-ku, Nagoya 464-8602, Japan.

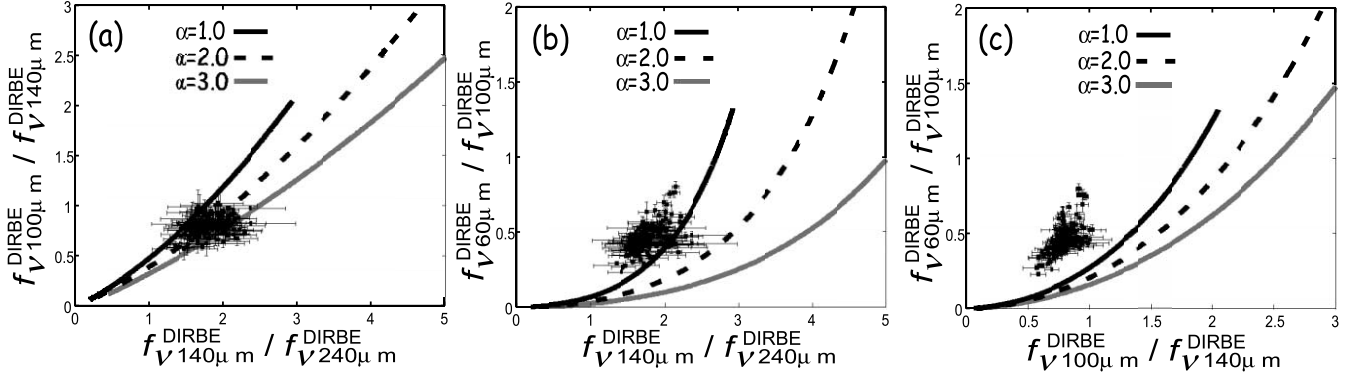


FIG. 1.— DIRBE color-color diagrams of (a) 100–140 μm vs. 140–240 μm , (b) 60–100 μm vs. 140–240 μm , and (c) 60–100 μm vs. 100–140 μm . Three model lines in each panel are calculated for the single graybody with fixed emissivity power-law indices of $\alpha = 1.0$, 2.0, and 3.0, taking account of the *COBE* DIRBE system spectral response curves $R_i(\lambda)$ and the color correction.

introduced the dust model of Li & Draine (2001) to explain the extinction curve in the LMC and suggested a smaller abundance of carbonaceous dust in the LMC than in the Milky Way.

Recently, Aguirre et al. (2003) derived the averaged flux in the LMC minus 30 Dor, 30 Dor alone, and the Small Magellanic Cloud (SMC) from the *COBE* DIRBE 100, 140, and 240 μm data and the TopHat submillimeter data sets of 630, 460, 400, and 245 GHz. They made a single graybody fit to the SED, deriving the typical dust equilibrium temperature of BGs $T_d = 25.0 \pm 1.8$ K and the emissivity power-law index $\alpha = 1.3$ for the LMC minus 30 Dor, $T_d = 26.2 \pm 2.3$ K and $\alpha = 1.50$ for 30 Dor alone, and $T_d = 29.5 \pm 2.7$ K and $\alpha = 0.91$ for the SMC. Compared with $18.6 < T_d < 24.7$ K and $\alpha = 2.0$ for the Milky Way (Reach et al. 1995), the LMC is generally in higher temperature environments for interstellar dust, which is supposed to result from the strong UV radiation field (Bel et al. 1986). Aguirre et al. (2003) did not resolve the various structures in the LMC but averaged them in bulk within 30 Dor and non-30 Dor regions. In this paper we analyze the infrared SED with higher spatial resolution based on the *IRAS* and *COBE* DIRBE databases and estimate the thermal emission of BGs from individual structures with different physical conditions.

Sauvage et al. (1990) did an *IRAS* band color analysis in terms of the effects of stellar age and metallicity on the infrared emission taking account of 50 pc scale structures in the LMC. They found a trend that those pixels with high $f(60)/f(100)$ and low $f(12)/f(25)$ are associated with young stars, while those with low $f(60)/f(100)$ and high $f(12)/f(25)$ are associated with old stars. This trend can be compared with the results reported by Helou (1986) for a number of galaxy samples that active starburst galaxies present high $f(60)/f(100)$ and low $f(12)/f(25)$ and that moderate cirrus-like ones exhibit low $f(60)/f(100)$ and high $f(12)/f(25)$. Sauvage et al. (1990) interpreted the trend in terms of a two-component model. In order to correctly interpret such characteristics in the *IRAS* colors among various structures in the LMC, we make further investigation on the properties of the infrared excess emission at 25 and 60 μm with respect to the FIR emission longer than 100 μm . Comparison with the FIR emission allows us to investigate the effects of BGs and VSGs separately in a quantitative way as was done for the Galactic plane (Sakon et al. 2004).

In this paper, we focus on the following issues: (1) the differences in the composition or the size distribution of diffuse interstellar dust between in the LMC and in the Milky Way, (2) the properties of the MIR excess emission in the LMC of various structures with different physical conditions, and (3) the

U^2 -proportional characteristics of the MIR excess emission, which provides us with an efficient measure to study the nature of distant objects from broadband photometry. Section 2 presents the calibration method of mid-infrared photometric data sets of the LMC. We investigate the fundamental properties of dust in the LMC in § 3. In § 4 we discuss the proper understanding of the infrared broadband photometric data sets of various astrophysical environments in the LMC using the latest SED model of interstellar dust. Finally, § 5 summarizes our conclusions.

2. DATA ANALYSIS

In this study, we use the *COBE* DIRBE Zodi-Subtracted Mission Average (ZSMA) data for 12, 25, 60, 100, 140, and 240 μm and the *IRAS* Sky Survey Atlas (ISSA) data for 12, 25, 60, and 100 μm in the LMC ($70^\circ 0' < \alpha_{\text{B1950.0}} < 90^\circ 0'$, $-72^\circ 0' < \delta_{\text{B1950.0}} < -65^\circ 0'$). These data contain, in addition to the LMC component, the Galactic foreground emission, which ought to be removed for the purpose of making careful analysis of dust properties peculiar to the LMC. We estimate the Galactic foreground infrared emission using the empirical correlation between the H I line intensity and the infrared emission (e.g., Lagache et al. 1998; Arendt et al. 1998). We derive the Magellanic H I intensity and the Galactic H I intensity separately according to their own radial velocity distributions: the Galactic component possesses velocities ranging from -100 to 50 km s $^{-1}$, while the LMC component ranges from 200 to 300 km s $^{-1}$. We derive the empirical relations between the integrated Galactic H I intensity from -100 to 50 km s $^{-1}$ and the infrared intensities in the region off the LMC, and then they are applied to the LMC region. Details of this procedure are described in Appendix A. In the following analysis we use only the data with signal-to-noise ratio (S/N) larger than 5 in all the infrared bands, where 1σ errors are estimated taking account of both the measurement errors ($\sigma_{\lambda,m}$) and the systematic errors in the process of the sky subtraction ($\sigma_{\lambda,s}$) as $\sigma_\lambda = (\sigma_{\lambda,m}^2 + \sigma_{\lambda,s}^2)^{1/2}$ for each band λ , where the subscript λ denotes 12, 25, 60, 100, 140, and 240 μm of the DIRBE bands (see Appendix A for details).

3. PROPERTIES OF FIR EMISSION IN THE LMC

The FIR emission from BGs in thermal equilibrium is often modeled by a single-temperature graybody $f_\nu^{\text{FIR}}(\lambda, T_d)$ given by

$$f_\nu^{\text{FIR}}(\lambda, T_d) = \tau(\lambda) B_\nu(\lambda, T_d), \quad (1)$$

where $\tau(\lambda)$ is the optical depth at λ and $B_\nu(T_d)$ is the Planck function of the temperature T_d . We assume that the dust emissivity is

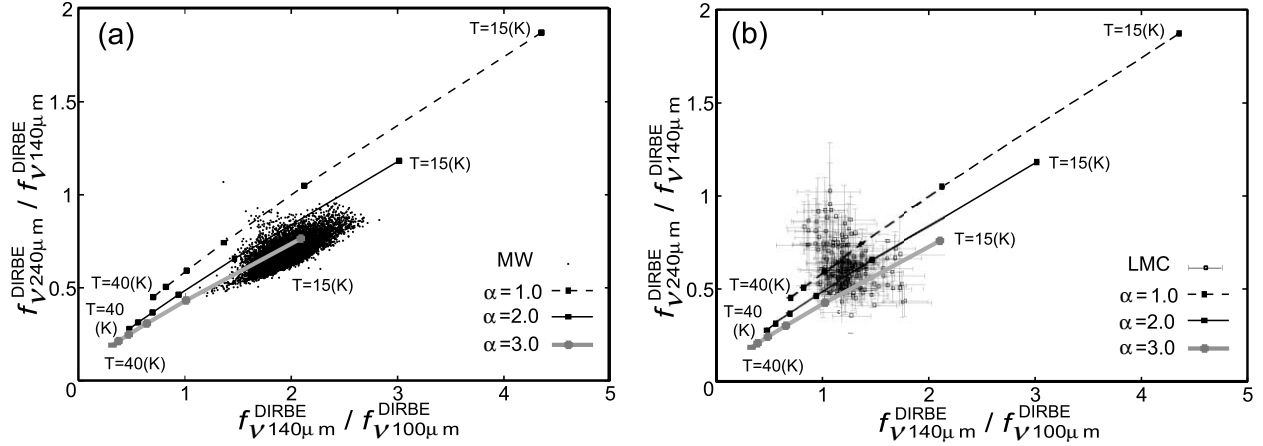


FIG. 2.—Color-color diagram of the DIRBE 240–140 μm color ($f_{V240\mu\text{m}}^{\text{DIRBE}}/f_{V140\mu\text{m}}^{\text{DIRBE}}$) vs. the 140–240 μm color ($f_{V140\mu\text{m}}^{\text{DIRBE}}/f_{V100\mu\text{m}}^{\text{DIRBE}}$) in the (a) inner Milky Way ($|l| < 60^\circ$, $|b| < 5^\circ$) and (b) LMC. Three model lines in both figures connect the points of eq. (1) calculated from 15 K in the top right to 40 K in the bottom left by a step of 5° for the fixed emissivity power-law indices of $\alpha = 1.0, 2.0$, and 3.0 .

proportional to $\lambda^{-\alpha}$. The data sets suitable for characterizing this emission are the *COBE* DIRBE maps in the far-infrared. The emission in the 60 μm band, which is important to constrain the Wien side of the graybody emission, is considerably contributed by the excess emission from VSGs.

Figure 1 shows the color-color diagrams made from the *COBE* DIRBE 60, 100, 140, and 240 μm maps in the LMC together with the model lines calculated for the single-temperature graybody emission with the emissivity power-law indices $\alpha = 1.0, 2.0$, and 3.0 , for which we derive the band intensity in the *COBE* DIRBE system by taking account of the *COBE* DIRBE system spectral response curves $R_i(\lambda)$ and the color correction. Most of the data in the diagram of the 100–140 μm color against the 140–240 μm color distribute in the regions of single-temperature graybodies of $\alpha = 1-3$ (see Fig. 1a); however, the diagrams of the 60–140 μm color against the 140–240 μm color and against the 100–140 μm indicate excess emission at the 60 μm band over single-temperature graybodies with the same α -values (see Figs. 1b and 1c). The emission at 60 μm cannot be accounted for consistently by single-temperature graybodies with those at 100, 140, and 240 μm and is likely to be attributed to excess emission due to VSGs, as in the diffuse Galactic objects (e.g., Désert et al. 1990; Shipman 1994; Finkbeiner et al. 2000). Thus, we use data at 100, 140, and 240 μm to estimate the properties of the thermal FIR emission.

Figure 2 shows the DIRBE color-color diagram of the 240–140 μm color against the 140–240 μm color in the LMC and that in the Galactic plane ($|l| < 60^\circ$, $|b| < 5^\circ$) as a reference. Figure 2 suggests that the emissivity power-law index in the LMC is generally smaller than that in the Milky Way, which is compatible with the results of Aguirre et al. (2003). In the following analysis, we discuss each model fitted with the emissivity power-law index of $\alpha = 1.0, 1.5$, and 2.0 for the LMC and with $\alpha = 2.0, 2.5$, and 3.0 for the Milky Way.

Another notable characteristic feature seen in Figure 2b is data that deviate from the model lines more significantly to the top left than the 1σ errors of the colors. The signal-to-noise ratios of these deviated data are 48.1 ± 18.5 at the 100 μm band, 7.2 ± 3.9 at the 140 μm band, and 9.8 ± 4.1 at the 240 μm band, while those of the other data are 46.5 ± 18.0 at the 100 μm band, 12.7 ± 6.4 at the 140 μm band, and 12.5 ± 6.2 at the 240 μm band on average. Therefore, the quality of the data does not significantly differ between the deviated data and the other data. The deviation from

the model line is within 2σ in most data, and thus further observations with better accuracy are needed to confirm the deviations. In the following analysis we treat these deviated data separately from the others in the manner described below to estimate the far-infrared intensity for these deviated data. Because of the small number of these data points, they do not affect the results of the present paper.

Excess emission at either 100 or 240 μm over a single component graybody is suggested to correspond to the deviated data. We look into the locations of these data points and plot them with white open circles in Figure 3. Some of them geometrically well correlate with the peripheries of supergiant shells (SGSs; Kim et al. 1998, 2003; Meaburn 1980; Yamaguchi et al. 2001a), especially at the edge of LMC 4 (see Fig. 3, SGS no. 4), for which

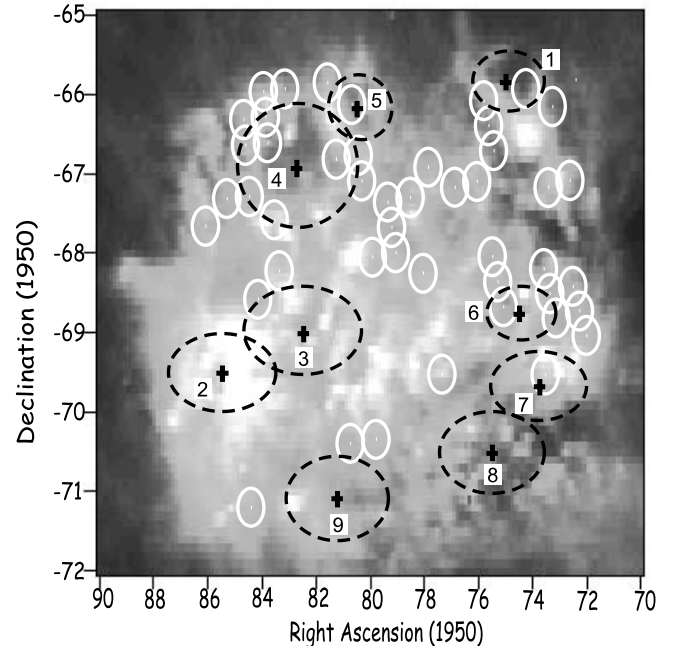


FIG. 3.—Distribution of the data points that deviate from the model lines (white open circles). The underlying map is the sky-subtracted *IRAS* 100 μm map. The dashed black circles in the map indicate the supergiant shells (SGSs) as numbered in Meaburn (1980).

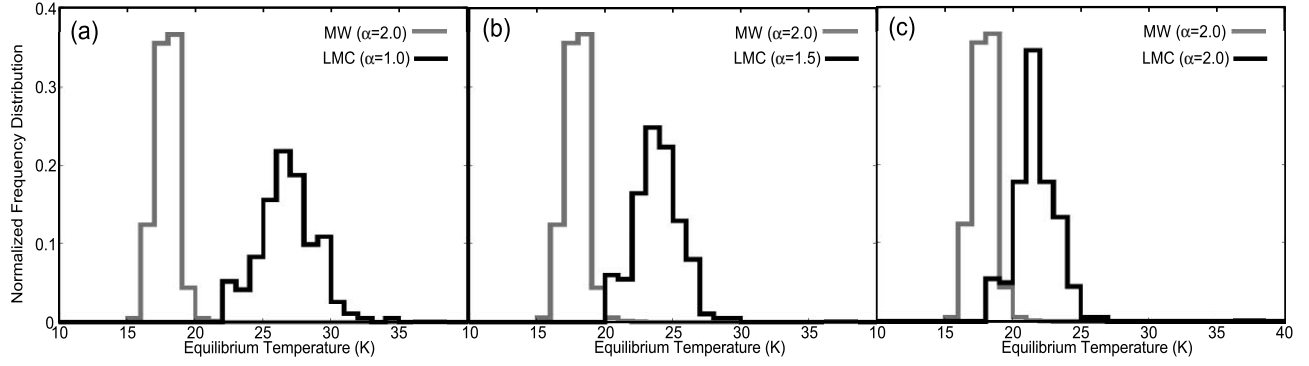


FIG. 4.— Histograms of the temperature of the warm dust T_w in the LMC obtained for (a) $\alpha_w = 1.0$, (b) 1.5, and (c) 2.0. Those in the Milky Way obtained for $\alpha_w = 2.0$ are overlaid in each panel as a reference.

Yamaguchi et al. (2001a) have suggested the presence of clumpy molecular clouds and evidence for triggered cluster formation. If the incident radiation field at those positions is weak, the thermal emission shifts to longer wavelengths and the temperature fluctuation component at $100 \mu\text{m}$ could become prominent. On the other hand, dust in such molecular clouds is shielded from the incident radiation and can become a cold component that effectively carries the excess at $240 \mu\text{m}$. We cannot determine which scenario more reasonably accounts for the deviated data points from only three bands at 100 , 140 , and $240 \mu\text{m}$.

As an additional constraint to evaluate the FIR emission, we introduce the correlation between the $12 \mu\text{m}$ band intensity and the FIR emission. The emission in the $12 \mu\text{m}$ band ($f_{\nu_{12 \mu\text{m}}}$) is carried partly by the UIR emission and partly by the excess emission from VSGs, whose intensity is proportional to the intensity of the incident radiation and the column density of the carriers. Therefore, $f_{\nu_{12 \mu\text{m}}}/F_{\text{FIR}}$ is supposed to be approximately constant if the carriers of both emissions coexist and are well mixed (Onaka 2000), which is actually found for most of the LMC other than the vicinity of young star clusters (see Fig. 6a, *open squares*). To make a quantitative estimate, we assume the excess emission at both 100 and $240 \mu\text{m}$ and a constant $f_{\nu_{12 \mu\text{m}}}/F_{\text{FIR}}$ for the deviated data and fit the SED with three components: a component in thermal equilibrium, cold dust in clumpy clouds contributing to $240 \mu\text{m}$, and VSGs contributing to $100 \mu\text{m}$. The following fit parameters are estimated for these deviated data: the fraction of the contribution of VSGs at $100 \mu\text{m}$ (ξ); the temperature of the warm and cold dust T_w and T_c , respectively; the opacity of the warm and cold dust at $140 \mu\text{m}$ $\tau_{140,w}$ and $\tau_{140,c}$, respectively; and the emissivity power-law indices of the warm and cold dust α_w and α_c , respectively. To reduce the number of free parameters we fix $\alpha_w = 1.0, 1.5$, or 2.0 and $T_c = 3, 6$, or 9 K , and α_c is fixed at 2.0 . For each of nine cases (combinations of $T_c = 3, 6$, or 9 K and $\alpha_w = 1.0, 1.5$, or 2.0), we determine four free parameters ξ , $\tau_{140,w}$, $\tau_{140,c}$, and T_w so that they reproduce the FIR SED provided by the DIRBE 100 , 140 , and $240 \mu\text{m}$ bands and so that $f_{\nu_{12 \mu\text{m}}}/F_{\text{FIR}}$ becomes the same as that averaged for the data other than those deviated values. As a result of the fit, we obtain $\xi = 7.1^{+11.6}_{-6.7} \%$ and $26.5^{+14.5}_{-13.8} \%$ as the contribution of cold dust in the DIRBE $240 \mu\text{m}$ band for the case of $\alpha_w = 1.5$ and $T_c = 6.0 \text{ K}$, for example. The results of the fit show that the contribution of cold dust in the DIRBE $240 \mu\text{m}$ band more effectively accounts for the deviated data in Figure 2b than the contribution of VSGs in the DIRBE $100 \mu\text{m}$ band.

As for the data that agree with the model lines in the two-color diagram within the 1σ errors, we assume a single-temperature

graybody with temperature T_w and an emissivity power-law index α_w of $1.0, 1.5$, or 2.0 . For each of three cases ($\alpha_w = 1.0, 1.5$, or 2.0) we derive two free parameters T_w and the opacity at $140 \mu\text{m}$ $\tau_{140,w}$ using a least-squares fit to the FIR SED of the DIRBE 100 , 140 , and $240 \mu\text{m}$ bands taking account of the errors in each band.

Figure 4 shows the temperature distribution of T_w for all the data in the LMC, for which three cases of $\alpha_w = 1.0, 1.5$, and 2.0 with $T_c = 6 \text{ K}$ are representatively calculated for the data deviated from the model lines to the top left in Figure 2b. We note that the data fitted with a single-temperature graybody occupy 82% of all the data in the LMC used in this analysis and that they dominate in the distribution peaks of T_w . The results of those calculated for the inner Galactic plane ($|l| < 60^\circ$, $|b| < 5^\circ$) are also shown in each plot with a gray line as a reference assuming a single graybody with temperature T_w and opacity at $140 \mu\text{m}$ $\tau_{140,w}$ for the case of fixed emissivity power-law index $\alpha_w = 2.0$. As has been indicated by Reach et al. (1995) and Aguirre et al. (2003), we have found higher equilibrium temperatures of the warm component and a wider temperature distribution in the LMC than for those in the Milky Way for whichever case we adopt. The characteristic of the FIR emission may relate to the nature of the carriers. Some types of amorphous silicate grains have smaller emissivity power-law indices at higher temperatures (Boudet et al. 2005). If such a kind of amorphous silicate is a dominant component of BGs in the LMC, it may partly or wholly account for the observed trend.

Table 1 summarizes the average temperatures of the warm dust and their 1σ ranges. We observe the various structures in the LMC separately from the almost face-on view, while the data in the Milky Way contain various structures in the line of sight and are averaged into similar values over any direction as far as only those in the inner Galaxy are concerned. This difference may account for the wider temperature distribution for the LMC. We have also made calculations with $T_c = 3$ and 9 K , and we confirm that T_c does not affect the results of the temperature of the warm component T_w . For comparison, the results by Aguirre et al. (2003) are shown in the last row of Table 1. The present results are in agreement with those of Aguirre et al. (2003).

It is difficult to determine the absolute value of α , since we cannot distinguish the emission from dust with various temperatures and large α from that with a single temperature and small α (Reach et al. 1995). In the following analysis, we use the integrated energy over the whole frequency carried by warm dust expediently expressed with a single graybody as F_{FIR} . The critical issue in our analysis is to properly estimate the emission carried by the warm dust or F_{FIR} . In this sense, the absolute value

TABLE 1
AVERAGE TEMPERATURE AND 1σ WIDTH OF THE DISTRIBUTION

Case	α_w	α_c	T_c (K)	T_w (K)	ΔT_w (K)
LMC					
1.....	1.0	2.0	3.0	26.6	2.1
2.....	1.0	2.0	6.0	26.7	2.1
3.....	1.0	2.0	9.0	26.8	2.1
4.....	1.5	2.0	3.0	23.8	1.7
5.....	1.5	2.0	6.0	23.8	1.7
6.....	1.5	2.0	9.0	23.9	1.7
7.....	2.0	2.0	3.0	21.6	1.4
8.....	2.0	2.0	6.0	21.6	1.4
9.....	2.0	2.0	9.0	21.7	1.4
Milky Way ^a					
1.....	2.0	17.9	0.8
2.....	2.5	16.5	0.7
3.....	3.0	15.4	0.6
LMC Minus 30 Dor ^b					
1.....	1.33 (± 0.07)	25.0	1.8

^a Data for the inner Galactic plane ($|l| < 60^\circ$, $|b| < 5^\circ$).

^b Values from Aguirre et al. (2003).

of the emissivity power-law index is less important, since it does not affect F_{FIR} in the first-order approximation.

4. DISCUSSION

We estimate the amount of excess emission at 12, 25, and 60 μm by subtracting the FIR emission in thermal equilibrium from the quoted intensities in the DIRBE ZSMA data set $I_{\nu_{12\mu\text{m}}}^{\text{quoted}}$, $I_{\nu_{25\mu\text{m}}}^{\text{quoted}}$, and $I_{\nu_{60\mu\text{m}}}^{\text{quoted}}$. We define the amount of the excess emission at 12, 25, and 60 μm as

$$I_{\nu_\lambda}^{\text{excess}} = I_{\nu_\lambda}^{\text{quoted}} - \frac{\int f_\nu^{\text{FIR}}(\nu, T_d) R_\lambda(\nu) d\nu}{\int (\nu_i/\nu) R_\lambda(\nu) d\nu}, \quad (2)$$

where the subscript λ denotes 12, 25, and 60 μm of the DIRBE bands and $R_\lambda(\nu)$ is the spectral response curve of the DIRBE λ μm bands. The 12 μm emission is carried by a series of the UIR bands from 11 to 14 μm , including some contribution from highly spiked VSGs, the 25 μm emission is most effectively carried by VSGs

heated to high temperatures, and the 60 μm emission is carried by VSGs stochastically heated to mild temperatures. Therefore, the amount of the excess emission is controlled by the strength and the hardness of the UV radiation field, as well as by the amount of VSGs and their size distribution. We compare the amount of the excess emission relative to the total FIR emission F_{FIR} in the LMC to that in the Milky Way. We integrate the emission from the warm component over the whole wavelength range to derive F_{FIR} :

$$F_{\text{FIR}} = \int_0^\infty \tau_\lambda B_\lambda(\lambda, T_w) d\lambda \\ = \tau_{140,w} \int_0^\infty \left(\frac{140 \mu\text{m}}{\lambda} \right)^\alpha B_\lambda(\lambda, T_w) d\lambda. \quad (3)$$

Figure 5 shows the distribution histogram of $\Delta\nu_{12\mu\text{m}} I_{\nu_{12\mu\text{m}}}^{\text{excess}}/F_{\text{FIR}}$, $\Delta\nu_{25\mu\text{m}} I_{\nu_{25\mu\text{m}}}^{\text{excess}}/F_{\text{FIR}}$, and $\Delta\nu_{60\mu\text{m}} I_{\nu_{60\mu\text{m}}}^{\text{excess}}/F_{\text{FIR}}$ in the LMC for the model of $\alpha_w = 1.5$ and $T_c = 6$ K, where $\Delta\nu_{12\mu\text{m}}$, $\Delta\nu_{25\mu\text{m}}$, and $\Delta\nu_{60\mu\text{m}}$ are the bandwidths of the DIRBE 12, 25, and 60 μm bands, respectively. For each model the mean values of the ratios of the excess emission to the FIR emission are summarized in Table 2.

The relative amount of the excess at 12 μm to F_{FIR} is smaller in the LMC than in the Galactic plane. This trend is consistent with the fact that the UIR emission in the Magellanic Clouds is relatively weak compared to that in our Galaxy (Vermeij et al. 2002; Li & Draine 2002). Figure 5b indicates a similar trend that the relative amount of the excess at 25 μm to F_{FIR} is smaller in the LMC than in our Galactic plane. From Figure 5c, on the contrary, the relative amount of the excess at 60 μm to F_{FIR} in the LMC is larger than that in our Galaxy. The relative trends between the LMC and our Galaxy do not change even if we adopt $\alpha = 2.0$ for the LMC and are almost insensitive to the temperature of the very cold dust T_c in the LMC.

If the size distributions of VSGs in the LMC and the Milky Way are similar to each other, each value of the excess-to- F_{FIR} ratios at 12, 25, and 60 μm should be the same between in the LMC and in the Milky Way. The present results suggest a paucity of relatively small sized VSGs in the LMC. The larger excess-to- F_{FIR} ratio at 60 μm in the LMC than in the Milky Way can be interpreted in terms of more abundant relatively large sized VSGs that effectively carry the excess emission in 60 μm in the LMC. Thus, the trends in Figure 5 suggest the size distribution of VSGs is skewed toward the large side in the LMC. We note, however, that the uncertainty in the emissivity power-law index α also affects the value of the ratio of the excess at 60 μm to F_{FIR} . It may

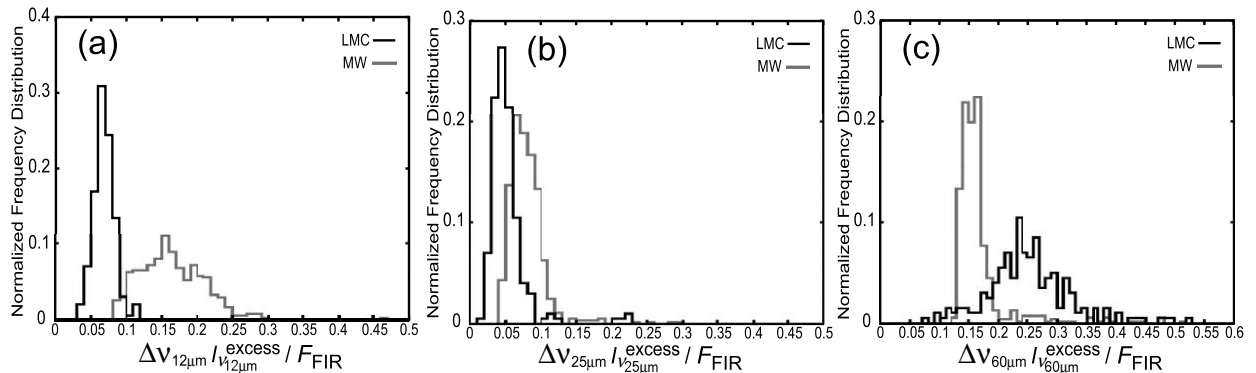


FIG. 5.—Histograms of (a) $\Delta\nu_{12\mu\text{m}} I_{\nu_{12\mu\text{m}}}^{\text{excess}}/F_{\text{FIR}}$, (b) $\Delta\nu_{25\mu\text{m}} I_{\nu_{25\mu\text{m}}}^{\text{excess}}/F_{\text{FIR}}$, and (c) $\Delta\nu_{60\mu\text{m}} I_{\nu_{60\mu\text{m}}}^{\text{excess}}/F_{\text{FIR}}$ in the LMC representatively calculated for the model of $\alpha_w = 1.5$ and $T_c = 6$ K with black lines and in the inner Milky Way calculated for the single-temperature graybody model of $\alpha_w = 2.0$ with gray lines.

TABLE 2
RELATIVE AMOUNT OF EXCESS EMISSION WITH VARIOUS PARAMETERS

Case	α_w	α_c	T_c (K)	$\Delta\nu_{12\mu m} I_{\nu_{12\mu m}}^{\text{excess}} / F_{\text{FIR}}$	$\Delta\nu_{25\mu m} I_{\nu_{25\mu m}}^{\text{excess}} / F_{\text{FIR}}$	$\Delta\nu_{60\mu m} I_{\nu_{60\mu m}}^{\text{excess}} / F_{\text{FIR}}$
LMC						
2.....	1.0	2.0	6.0	0.065 ± 0.014	0.050 ± 0.028	0.215 ± 0.067
4.....	1.5	2.0	3.0	0.068 ± 0.014	0.053 ± 0.029	0.252 ± 0.073
5.....	1.5	2.0	6.0	0.068 ± 0.014	0.053 ± 0.029	0.252 ± 0.073
6.....	1.5	2.0	9.0	0.068 ± 0.014	0.053 ± 0.029	0.249 ± 0.077
8.....	2.0	2.0	6.0	0.071 ± 0.015	0.055 ± 0.031	0.282 ± 0.080
Milky Way ^a						
1.....	2.0	0.164 ± 0.045	0.080 ± 0.027	0.169 ± 0.050
2.....	2.5	0.171 ± 0.047	0.083 ± 0.028	0.182 ± 0.054
3.....	3.0	0.176 ± 0.048	0.086 ± 0.029	0.190 ± 0.057

^a Data for the inner Galactic plane ($|l| < 60^\circ$, $|b| < 5^\circ$).

be possible that the shallower emissivity profile or α smaller than unity may account for part of the larger ratio in the LMC. The uncertainty, however, does not affect the results at 12 and 25 μm , and thus it is a secure conclusion that the amount of small-sized VSGs relative to that of BGs is smaller in the LMC than in the Milky Way.

4.1. Relation between the Excess Emission and F_{FIR}

The mid- to far-infrared SED is determined in the context of the size distributions of VSGs and BGs, their compositions, and their abundances in a certain interstellar radiation environment. As for the Galactic plane, Sakon et al. (2004) have reported bipolar sequences in the plots of DIRBE 60–100 μm color against the dust temperature in thermal equilibrium derived from the DIRBE 100–140 μm color. They found that the steeply increasing linear branch comprises the data in the Galactic plane ($|b| < 1.2^\circ$) while the horizontal branch comprises the data off the Galactic plane. We use the excess-to- F_{FIR} ratios instead of the colors of 12, 25, and 60–100 μm for the purpose of better analyzing the characteristics of the data in the LMC, since the emission at 100 μm depends on the temperature monochromatically while the emission at 12, 25, and especially 60 μm contains, more or less, the thermal emission from BGs. The plots of the excess-to- F_{FIR} ratios against T_w in the LMC again present bipolar sequences particularly in those for 25 and 60 μm (Fig. 6). Based on the positional analysis of the data on the steeply rising linear branch, we have found that these data include young star clusters ($t_c < 30$ Myr) classified as SWB type 0 with $t_c < 10$ Myr and type I with $10 \text{ Myr} < t_c < 30$ Myr (Searle et al. 1980; Bica et al. 1996), where t_c is the age of the star cluster. In Figure 6 we have plotted the excess-to- F_{FIR} ratios against T_w at SWB type 0 and type I cluster positions (*filled diamonds*) separately from those at other regions located at least 20' away from any SWB type 0 and type I clusters (*open circles*). The former data points clearly form a clear steeply rising linear branch for 25 and 60 μm . The 12 μm data also show a trend of the rising branch around $T_w = 25$ K, although it is less pronounced than the emission at 25 and 60 μm .

Since DIRBE's beam size of 42' in diameter is too large to grasp peculiar environments around young star clusters, we use the ISSA data sets from which the foreground Galactic emission is subtracted for further investigation of the properties of VSGs and BGs around young star clusters. For this purpose, we need a grid of the data of F_{FIR} or T_w with a spatial resolution comparable to that of the ISSA data set. We adopt an empirical

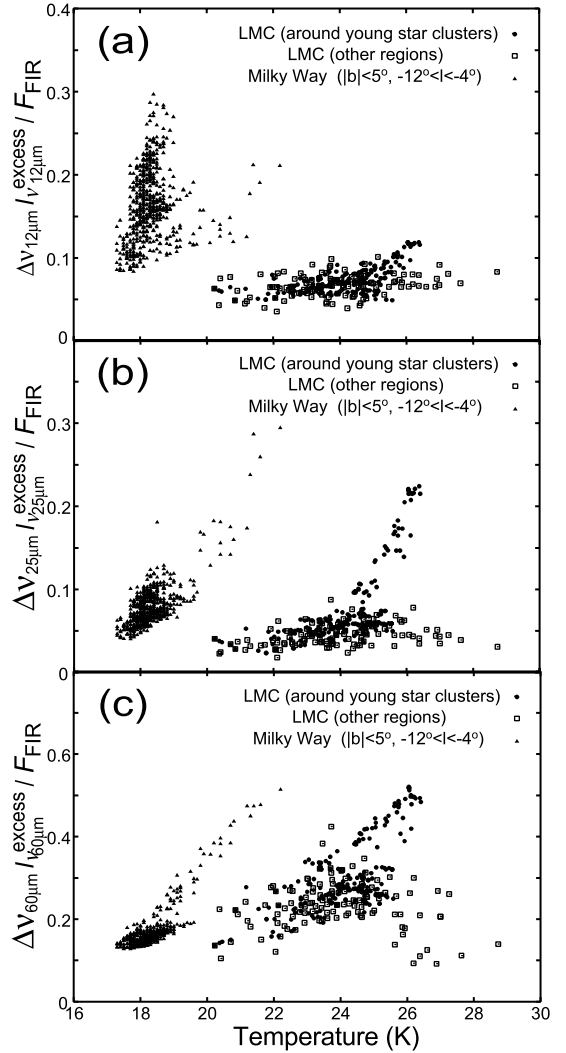


FIG. 6.—Plots of (a) $\Delta\nu_{12\mu m} I_{\nu_{12\mu m}}^{\text{excess}} / F_{\text{FIR}}$, (b) $\Delta\nu_{25\mu m} I_{\nu_{25\mu m}}^{\text{excess}} / F_{\text{FIR}}$, and (c) $\Delta\nu_{60\mu m} I_{\nu_{60\mu m}}^{\text{excess}} / F_{\text{FIR}}$ against dust temperature. The data around young star clusters ($t_c < 30$ Myr) in the LMC are shown with filled diamonds, those without any young star clusters in the LMC are shown with open squares, and those in the inner Milky Way ($|b| < 5^\circ$ and $-12^\circ < |l| < -4^\circ$) are shown with filled triangles for comparison.

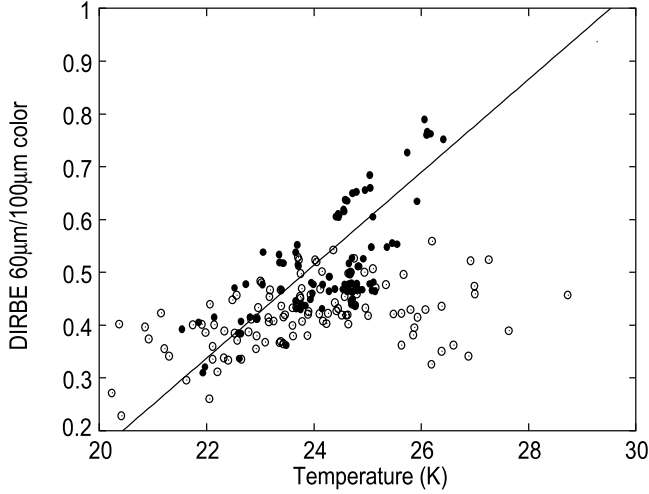


FIG. 7.— The $60\ \mu\text{m}/100\ \mu\text{m}$ color-to-temperature relation from the DIRBE data in the LMC. The filled diamonds correspond to the data including young SWB type 0 clusters, and the open circles correspond to those without young star clusters (neither SWB type 0 nor SWB type 1). The linear fit to the former data is also shown by the solid line.

temperature-to- $60\ \mu\text{m}/100\ \mu\text{m}$ relation (Nagata et al. 2002; Sakon et al. 2004; Hibi et al. 2006) derived from the DIRBE data set in the LMC and apply it to the ISSA data. This empirical relation synthetically treats the emission emitted by both the BGs in thermal equilibrium and the stochastically heated VSGs in the $60\ \mu\text{m}$ band.

We derive the empirical relation between the temperature and the $60\ \mu\text{m}/100\ \mu\text{m}$ using the DIRBE flux at SWB type 0 cluster positions. We define the DIRBE flux at a certain SWB type 0 cluster by averaging the DIRBE data with a weight of $(1/\delta d)^2$ for $\delta d < 21'$, where δd is the distance from the cluster position. Figure 7 shows the plot of the DIRBE $60\ \mu\text{m}/100\ \mu\text{m}$ color against T_w , in which the data at SWB type 0 clusters (filled diamonds) comprise a linear sequence, while the data located at least $21'$ away from the SWB type 0 and SWB type 1 positions (open circles) comprise a flat sequence. We fit the former data with a linear function,

$$\frac{I_{\text{DIRBE}}^{60\ \mu\text{m}}}{I_{\text{DIRBE}}^{100\ \mu\text{m}}} = \zeta T_w + \eta, \quad (4)$$

which we use as the empirical temperature-to- $60\ \mu\text{m}/100\ \mu\text{m}$ relation for regions with young star clusters in the LMC. The best-fit parameters are listed in Table 3 together with those parameters derived in Nagata et al. (2002) for the entire Galactic plane data for comparison. The slopes (ζ) are in fair agreement with each other.

The calibration for the ISSA 60 and $100\ \mu\text{m}$ data against the DIRBE 60 and $100\ \mu\text{m}$ data is summarized in Appendix B. With this calibration the ISSA data are transformed into the DIRBE system, and we apply equation (4). Then we obtain the dust temperature T_w and the optical depth at $100\ \mu\text{m}$ τ_{100} at each SWB type 0 position with the ISSA spatial resolution, where the ISSA flux at the SWB type 0 positions is derived by averaging the ISSA data within $2'$ from each cluster position with a weight of $(\delta d)^2$. The total FIR emission F_{FIR} and the amount of the excess emission at 12 and $25\ \mu\text{m}$, $\Delta\nu_{12\ \mu\text{m}}^{\text{IRAS}} I_{\text{IRAS}}^{\text{excess}}$ and $\Delta\nu_{25\ \mu\text{m}}^{\text{IRAS}} I_{\text{IRAS}}^{\text{excess}}$, respectively, are calculated by equations similar to equations (2) and (3), where $\Delta\nu_{12\ \mu\text{m}}^{\text{IRAS}}$ and $\Delta\nu_{25\ \mu\text{m}}^{\text{IRAS}}$ are the bandwidth of IRAS 12 and $25\ \mu\text{m}$ bands, respectively.

TABLE 3

PARAMETERS OF THE EMPIRICAL TEMPERATURE-TO- $60\ \mu\text{m}/100\ \mu\text{m}$ RELATION

Target	ζ	η
LMC.....	0.088 ± 0.007	-1.60 ± 0.17
Milky Way ^a	0.085 ± 0.009	-1.17 ± 0.12

NOTE.—See eq. (4).

^a From Nagata et al. (2002).

Figure 8 plots the ratios of the excess emission at 12 and $25\ \mu\text{m}$ to FIR against the dust temperature around young star clusters. For regions without star clusters, we assume that the COBE beam size is adequate enough to discuss the average properties of the mid- to far-infrared SED. Instead of obtaining T_w at each IRAS data position, we directly degrade the IRAS data into the DIRBE beam size and then use T_w obtained from the DIRBE analysis in order to reduce the systematic calibration errors. As indicated in Figure 7 these data form a horizontal branch. We show the average value of the ratios of the excess emission at 12 and $25\ \mu\text{m}$ to FIR for regions without star clusters (solid lines) with the $1\ \sigma$ deviation ranges (dotted lines) in each panel. As for $25\ \mu\text{m}$ (see Fig. 8b) we can clearly recognize that a steeply rising linear branch is formed by the data for the SWB type 0 cluster positions. As for $12\ \mu\text{m}$ (see Fig. 8a) the data for the SWB type 0 cluster positions do not seem to form a steeply rising linear branch and distribute around those of the regions without star clusters. We conclude that the depression of the 12 – $25\ \mu\text{m}$ color around young star clusters found by Sauvage et al. (1990) can be attributed to an increase of the $25\ \mu\text{m}$ flux in the strong radiation field rather than to a decrease in the $12\ \mu\text{m}$ flux due to the destruction of the UIR band carriers. The nature of the bipolar sequences is further discussed in the next section.

4.2. Dust SED Model Analysis of the LMC

Recently, Tokura et al. (2005) have proposed a model to account for the linearly rising branch of the Galactic plane in terms of the superposition of dust emissions (Takagi et al. 2003) under different radiation field strengths in the line of sight and/or within the beam. We apply this model to the LMC. The interstellar radiation field (ISRF) is assumed to be given by scaling that estimated for our Galaxy (Mathis et al. 1983). The scale factor is defined by U , and $U = 1$ corresponds to the solar vicinity value. Then we assume the distribution of the ISRF as

$$f(U) \propto U^{-\beta} \quad \text{for } U_{\min} < U < U_{\max}, \quad (5)$$

where β is the power-law index that determines the relative contributions of different radiation field intensities and U_{\min} is the minimum value and U_{\max} the maximum value of the intensity scale factor of the ISRF in the line of sight (e.g., Dale et al. 2001). Figure 9 shows that the steeply rising branch can be reproduced by the model line to trace β with constant $(U_{\min}, U_{\max}) = (1, 10^5)$, while the horizontal branch can be reproduced by the model line to trace β with constant $(U_{\min}, U_{\max}) = (0.5, 100)$. The model lines do not exactly fit with the observations, but they account for the observed trend fairly well. The difference may be attributed to the variation in the dust size distribution, whose fine adjustment is beyond the scope of the present paper. Here we point out that the general characteristics observed can be accounted for by this superposition model. In this model, the steeply rising branch is interpreted in terms of the increase in β with a nearly

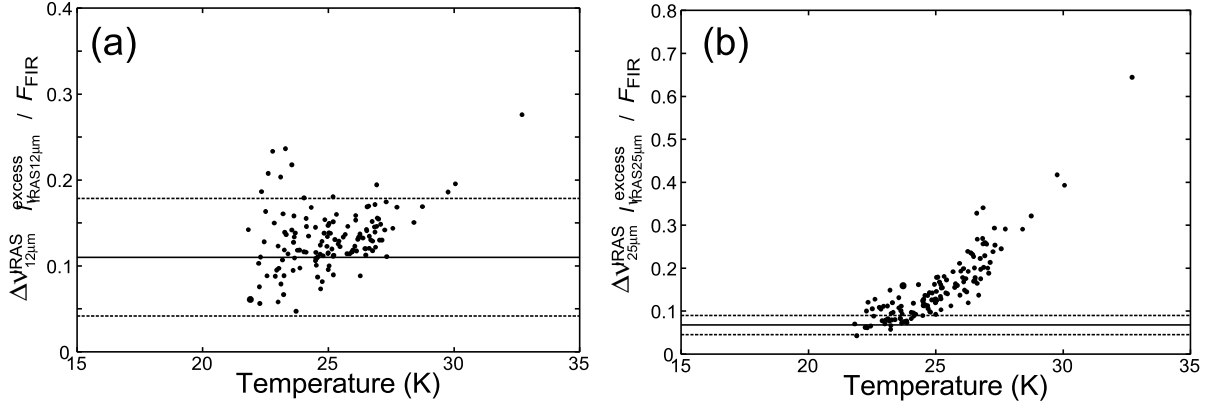


FIG. 8.—Plots of (a) $\Delta\nu_{12\mu\text{m}}^{IRAS} I_{\nu_{IRAS\ 12\mu\text{m}}}^{\text{excess}} / F_{\text{FIR}}$ and (b) $\Delta\nu_{25\mu\text{m}}^{IRAS} I_{\nu_{IRAS\ 25\mu\text{m}}}^{\text{excess}} / F_{\text{FIR}}$ derived from the ISSA data against dust temperature for the data around young star clusters ($t_c < 30$ Myr) in the LMC (filled diamonds). The average values of $\Delta\nu_{12\mu\text{m}}^{IRAS} I_{\nu_{IRAS\ 12\mu\text{m}}}^{\text{excess}} / F_{\text{FIR}}$ and $\Delta\nu_{25\mu\text{m}}^{IRAS} I_{\nu_{IRAS\ 25\mu\text{m}}}^{\text{excess}} / F_{\text{FIR}}$ for diffuse regions without young star clusters are shown by the solid lines with the dotted lines for the 1σ deviation range.

constant (large) U_{max} . These data correspond to regions that contain young star clusters, which provide large U_{max} in the beam. The present model accounts for the rising branch if the luminosity of the star cluster does not appreciably vary from cluster to cluster (constant U_{max}), and the value of β decreases with the increase in the contribution of the cluster. The absence of young star clusters in the beam narrows the range between U_{min} and U_{max} , resulting in the horizontal branch. The bimodal characteristics are controlled by U_{max} or the presence or absence of young star clusters in the beam.

4.3. Properties of MIR Emission in CO Molecular Clouds

In the previous section we focus on the properties of the MIR excess emission in regions with active star formation. In this section we investigate the properties of the MIR SED in CO molecular clouds without star formation activities using the ISSA data set and the $^{12}\text{CO}(J=1 \rightarrow 0)$ survey data at $\lambda = 2.7$ mm taken by NANTEN, a 4 m millimeter-wave telescope of Nagoya University at Las Campanas Observatory. It has a half-power beam-width (HPBW) of $2.6'$ at 115 GHz (Ogawa et al. 1990; Fukui & Sakakibara 1992). The spatial resolution of the CO data is degraded into $4' \times 4'$ to match with the *IRAS* beam size. We use only the data more than $16'$ (about 200 pc) away from any of the SWB type 0 and SWB type 1 members. We also exclude the *IRAS* point sources listed in the *IRAS* Point Source Catalog, version 2.1

(PSC) in order to avoid their contribution to the infrared color analysis on the diffuse interstellar medium (ISM) in the LMC. Since these data come from molecular clouds in various locations in the LMC, we need to examine the environment where they exist and treat those populations with different physical conditions separately in order to understand the individual properties of the MIR SED in CO molecular clouds.

In the plot of the 60–100 μm color ($f_{\nu_{60\mu\text{m}}} / f_{\nu_{100\mu\text{m}}}$) against $I_{12\text{CO}}$, we find roughly three populations with different values of the 60–100 μm color (see Fig. 10a). We classify the populations with $f_{\nu_{60\mu\text{m}}} / f_{\nu_{100\mu\text{m}}} < 0.24$ into bin I, those with $0.24 < f_{\nu_{60\mu\text{m}}} / f_{\nu_{100\mu\text{m}}} < 0.34$ into bin II, and those with $f_{\nu_{60\mu\text{m}}} / f_{\nu_{100\mu\text{m}}} > 0.34$ into bin III. We examine the locations of the members of each group in the LMC and plot them in Figures 10b–10d. We find that bin I consists of molecular clouds located at the southeast end of the CO arc, bin II mainly includes molecular clouds in the molecular ridge, and bin III consists of molecular clouds including those located near the 30 Dor complex (Fukui et al. 1999, 2002).

Figure 11a is a plot of the *IRAS* 12–25 μm color ($f_{\nu_{12\mu\text{m}}} / f_{\nu_{25\mu\text{m}}}$) against the CO intensity $I_{12\text{CO}}$ for CO molecular clouds that are detected with $>3\sigma$ in the LMC. Large scatter in the 12–25 μm color is found for $I_{12\text{CO}}$ smaller than 8 K km s^{-1} . Figures 11b–11d show the plots of the 12–25 μm color against $I_{12\text{CO}}$ for data that belong to bins I, II, and III, respectively. We find the average value of the 12–25 μm color at small $I_{12\text{CO}}$ in bin I is the highest,

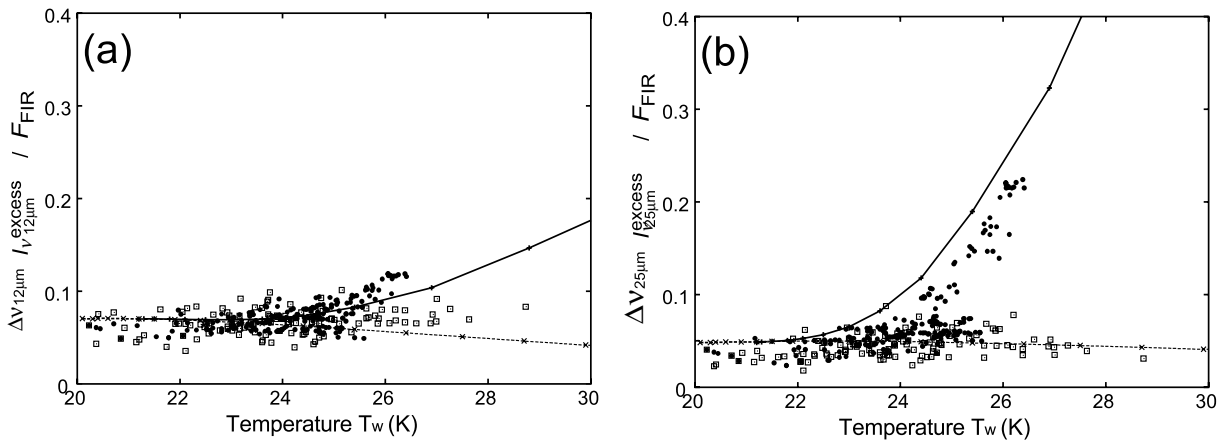


FIG. 9.—Plots of (a) $\Delta\nu_{12\mu\text{m}}^{IRAS} I_{\nu_{12\mu\text{m}}}^{\text{excess}} / F_{\text{FIR}}$ and (b) $\Delta\nu_{25\mu\text{m}}^{IRAS} I_{\nu_{25\mu\text{m}}}^{\text{excess}} / F_{\text{FIR}}$ against dust temperature T_w . The model results are also shown for $(U_{\text{min}}, U_{\text{max}}) = (1, 10^5)$ by the solid lines and for $(U_{\text{min}}, U_{\text{max}}) = (0.5, 10^2)$ by the dashed lines. The ticks on the line correspond to $\beta = 3.0$ for lower T_w and to $\beta = 1.0$ for higher T_w by steps of 0.1. The symbols are the same as those in Fig. 6.

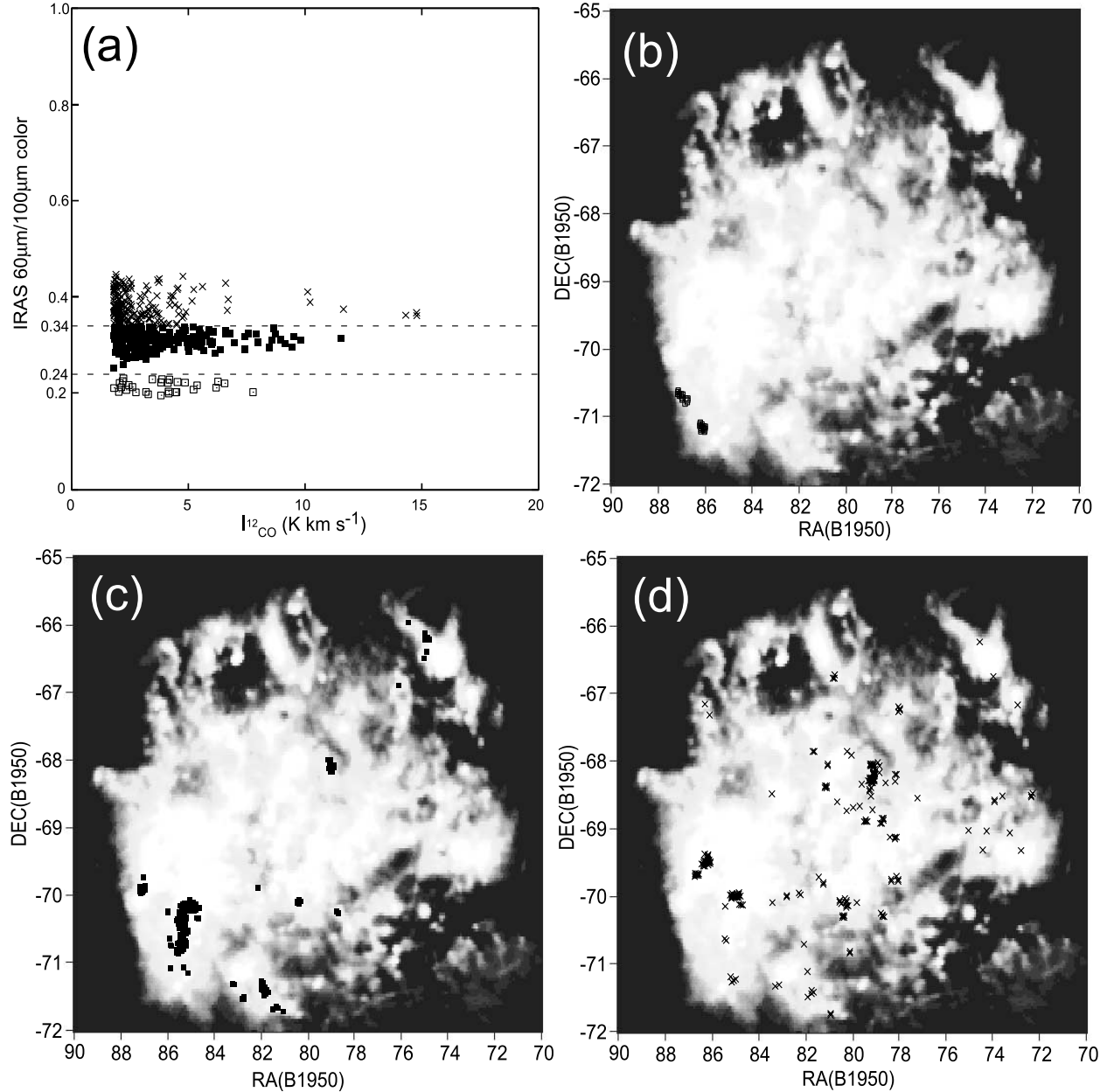


FIG. 10.—(a) Plot of the IRAS 60–100 μm color ($f_{\nu 60 \mu\text{m}}/f_{\nu 100 \mu\text{m}}$) against $I_{12\text{CO}}$. The data are classified as bin I (open squares), bin II (filled squares), and bin III (crosses; see text). (b–d) Distribution of data in bin I, bin II, and bin III, respectively. The underlying map is the sky-subtracted IRAS 100 μm map.

whereas the average value of the 60–100 μm color is the lowest among the three bins. On the other hand, we find the average value of the 12–25 μm color at small $I_{12\text{CO}}$ in bin III is the lowest, whereas that of the 60–100 μm color is the highest.

Since we still see large scatter in the 12–25 μm color at small $I_{12\text{CO}}$ especially in bins II and III, we make detailed analysis of the CO molecular clouds in the CO molecular ridge and the CO arc separately (Mizuno et al. 2001) in order to further investigate the properties of the 12–25 μm color in individual CO molecular clouds, where the CO molecular ridge and the CO arc are the structure extending southeast to the 30 Dor complex (Fig. 12). We analyze six regions separately (arc I, arc II, arc III, molecular ridge north, molecular ridge center, and molecular ridge south; see Fig. 12). Molecular clouds in arc III in the CO arc belong to bin III and are located close to the 30 Dor complex, those in arc II in the CO arc belong to bin II, and those in arc I in the CO arc belong to bin I and are located in rather quiet environments. Mo-

lecular clouds in molecular ridge north, molecular ridge center, and molecular ridge south belong to bin II, and molecular ridge north is located at the nearest region to the 30 Dor complex among the three. Yamaguchi et al. (2001b) report the presence of compact H II regions associated with the molecular clouds in molecular ridge center. Figures 13a–13f are the plots of the 12–25 μm color against $I_{12\text{CO}}$ in arc III, molecular ridge north, arc II, molecular ridge center, arc I, and molecular ridge south, respectively. In Table 4, the average and the standard deviation of the 12–25 μm color in the molecular clouds within each of these six regions are summarized. We characterize the behavior of the 12–25 μm color in CO clouds in terms of the fit with $f_{\nu 12 \mu\text{m}}/f_{\nu 25 \mu\text{m}} = \phi I_{12\text{CO}} + \psi$, where ϕ is the slope and ψ is the offset (Fig. 13).

We find mild trends of the 12–25 μm color against $I_{12\text{CO}}$ in arc III with a positive slope $\phi = (6.2 \pm 2.4) \times 10^{-3} \text{ K}^{-1} \text{ km}^{-1} \text{ s}$ (Fig. 13a) and in molecular ridge north with $\phi = (14.2 \pm 5.7) \times 10^{-3} \text{ K}^{-1} \text{ km}^{-1} \text{ s}$ (Fig. 13b), both of which are located close

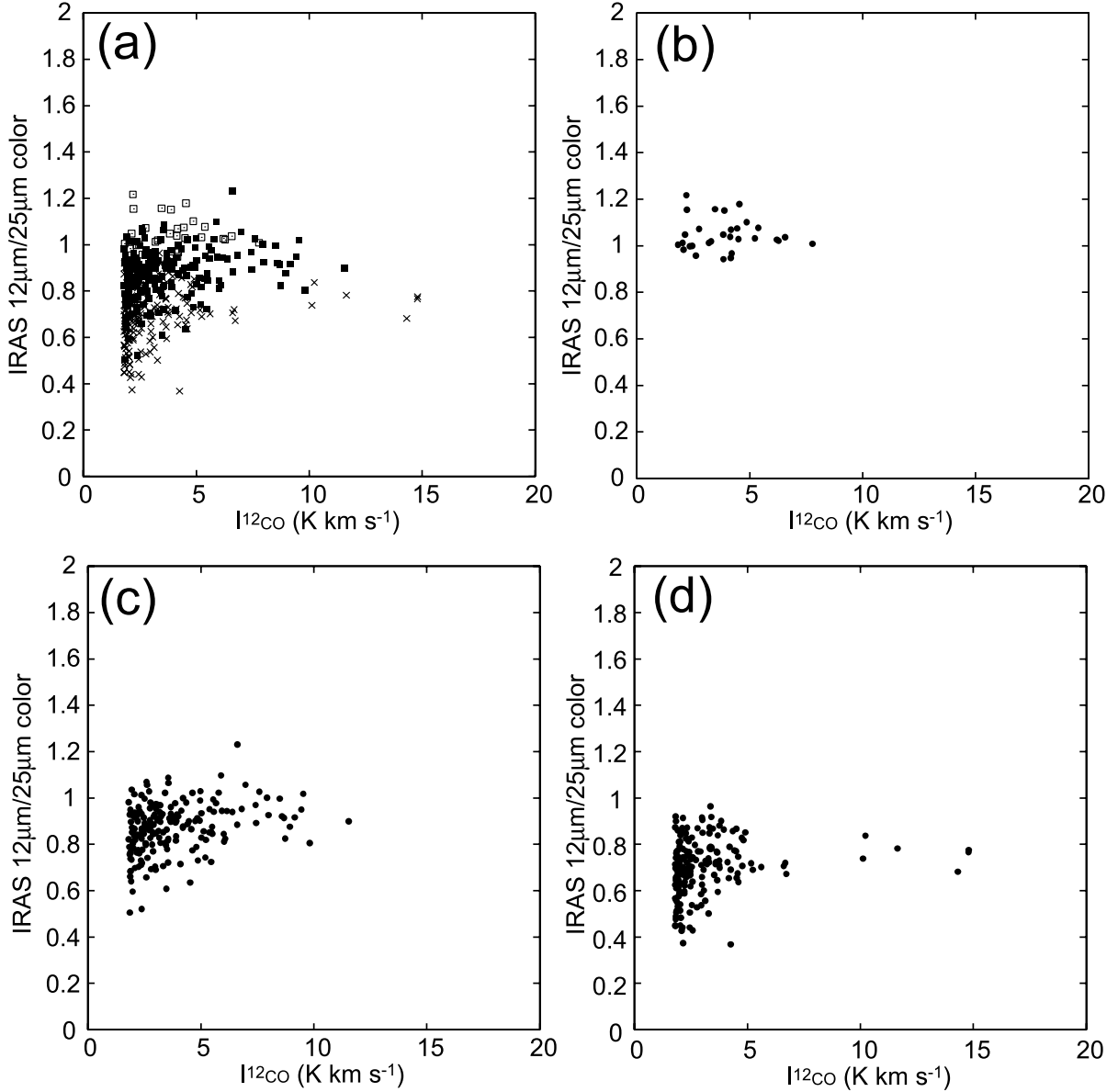


FIG. 11.—(a) Plot of the *IRAS* 12–25 μm color ($f_{12\mu\text{m}}/f_{25\mu\text{m}}$) against $I_{12\text{CO}}$ for all the data used in this analysis. Those in bin I are shown with open squares, those in bin II with filled squares, and those in bin III with crosses. (b) Data in bin I; (c) data in bin II; (d) data in bin III.

to the 30 Dor complex. On the other hand, the plots of the 12–25 μm color against $I_{12\text{CO}}$ in arc I and in molecular ridge south, which are located far from the 30 Dor complex, show smaller slopes $\phi = (-2.1 \pm 8.6) \times 10^{-3}$ (Fig. 13e) and $(-6.1 \pm 10.5) \times 10^{-3} \text{ K}^{-1} \text{ km}^{-1} \text{ s}$ (Fig. 13f), respectively. We also find that the slope ϕ decreases and the offset ψ increases from molecular ridge north to molecular ridge south and from arc III to arc I, which corresponds to the increase in distance from 30 Dor.

We consider again the superposition of dust emission under different ISRFs to understand the characteristics of the MIR SED in the CO molecular clouds. In this case, we assume the ISRF outside the molecular cloud gives U_{max} of equation (5) and that inside the molecular cloud gives U_{min} . Typical giant molecular clouds (GMCs) in the LMC have radii ranging from 28 to 105 pc (Mizuno et al. 2001), which are comparable to the *IRAS* beam size. Since each cloud is supposed to have fine structures and ^{12}CO is optically thick, $I_{12\text{CO}}$ measures the surface density of CO molecular clouds within the beam. Regions with small $I_{12\text{CO}}$ have low surface density of CO molecular clouds and small β in equa-

tion (5), while those with large $I_{12\text{CO}}$ have high surface density of CO molecular clouds and thus large β . In this interpretation an increase in $I_{12\text{CO}}$ corresponds to an increase in β .

Inside a dense molecular cloud interstellar UV photons are shielded due to extinction (Tielens & Hagen 1982; d’Hendecourt et al. 1985) and the temperature of BGs becomes low (e.g., 13 K for the CO cloud in Ursa Major cirrus; Miville-Deschênes et al. 2002). We set $U_{\text{min}} = 0.1$ to represent the typical ISRF inside the CO molecular cloud. Figure 14 shows the model profiles of the 12–25 μm color against β for $(U_{\text{min}}, U_{\text{max}}) = (0.1, 10)$, $(0.1, 100)$, and $(0.1, 1000)$. For larger U_{max} , the 12–25 μm color declines more deeply at small β , indicating that the effect of the ISRF outside the CO cloud becomes significant for small $I_{12\text{CO}}$. On the other hand, for smaller U_{max} ($\simeq 10$), the 12–25 μm color hardly decreases even at small β and the 12–25 μm color is insensitive to β .

Molecular clouds in arc III and in molecular ridge north typically have large 60–100 μm color (see Table 4). They are located in the vicinity of the 30 Dor complex, and the ISRF outside these CO molecular clouds is strong. The trends of the 12–25 μm color

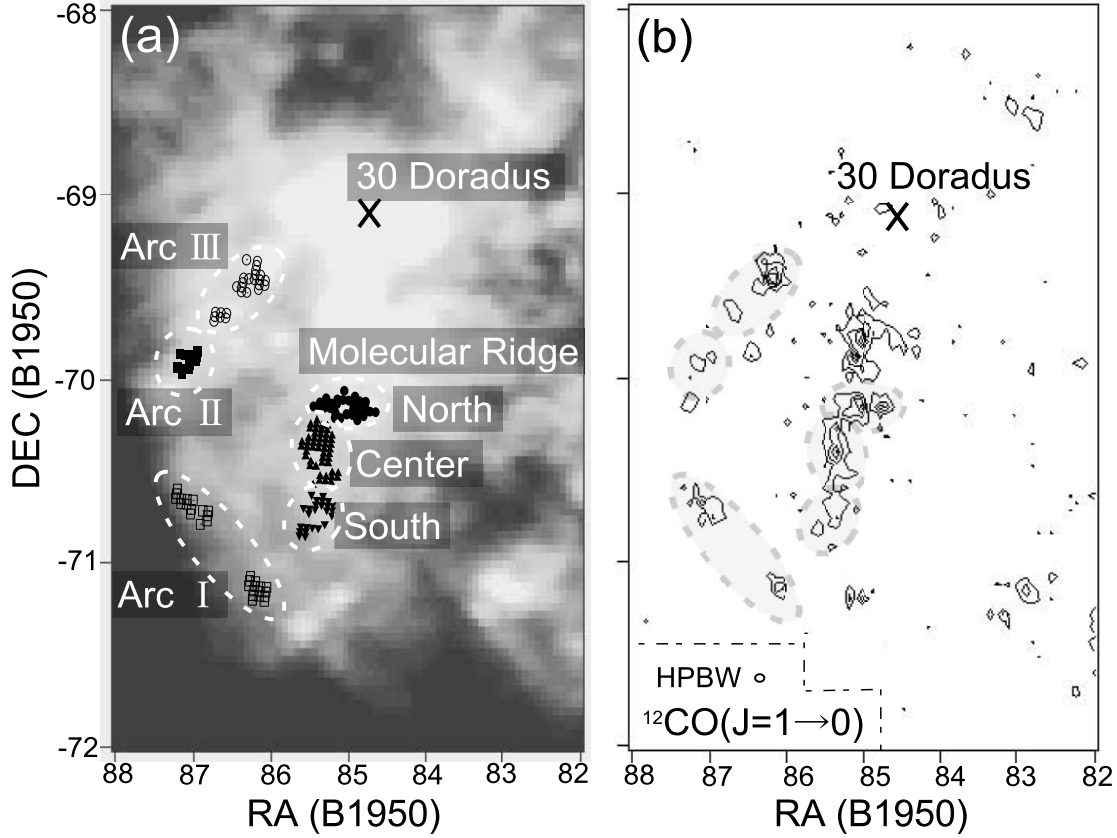


FIG. 12.—(a) Local structures in the molecular ridge and the CO arc in the LMC. Several CO cloud positions are shown on the sky-subtracted $100\mu\text{m}$ map. Arcs I–III are CO molecular clouds in the CO arc classified into bins I–III, respectively; molecular ridges north, center, and south are CO molecular clouds in the northern, central, and southern parts of the molecular ridge classified into bin II. (b) NANTEN ^{12}CO intensity of the corresponding region shown with contours with a 2 K km s^{-1} step.

against $I_{12\text{CO}}$ with a positive slope ϕ in these clouds are reasonably accounted for by large U_{max} (Fig. 14). On the other hand, molecular clouds in arc I and in molecular ridge south have small $60\text{--}100\mu\text{m}$ color. They are located far from the 30 Dor complex, and the ISRF outside the CO molecular clouds is weak. The constancy of the $12\text{--}25\mu\text{m}$ color can be accounted for by small U_{max} (e.g., $U_{\text{max}} = 10$; Fig. 14). Consequently, the decrease in the slope ϕ and the increase in the offset ψ from molecular ridge north to molecular ridge south and from arc III to arc I can directly be explained in terms of a decrease in U_{max} . Large scatter in Figure 10a at small $I_{12\text{CO}}$ can be attributed to the contribution from molecular clouds at various locations with different U_{max} .

In dense CO molecular clouds, large grains may be preferably formed through coagulation of small dust grains on large grains (Bernard et al. 1999), which may result in reduction of the abundance of small grains. This would decrease the UIR emission in dense CO clouds as suggested in Miville-Deschênes et al. (2002) for the Ursa Major cirrus cloud. It may explain the trends of possible negative slopes ϕ in Figures 13e and 13f.

For further analysis on the properties of polycyclic aromatic hydrocarbons (PAHs) and VSGs in CO molecular clouds, MIR spectroscopic observations using *AKARI* (Murakami 2004) and/or *Spitzer* (Werner et al. 2004) would be valuable. We note that ^{13}CO observations will be important to further discuss the properties of interstellar dust in molecular clouds, since ^{13}CO is optically thin and $I_{13\text{CO}}$ can directly measure the density of the CO molecular cloud.

5. SUMMARY

We have investigated the properties of mid- to far-infrared emission in the Large Magellanic Cloud (LMC) based on the

COBE DIRBE and the ISSA data sets. The Galactic foreground emission has been estimated from the correlations between the H I data and the infrared intensities and subtracted. Based on the two-color diagram analysis of the *COBE* DIRBE $240\text{--}140\mu\text{m}$ color against the $140\text{--}100\mu\text{m}$, we find that the typical value of the emissivity power-law index α in the LMC is smaller than that in the Milky Way. We find some data that are deviated from model predictions in the diagram. They can be interpreted as excess at $100\mu\text{m}$ and/or at $240\mu\text{m}$, and some of these data are located at the periphery of supergiant shells. Next, we estimate the amount of the MIR excess emission in the 12 , 25 , and $60\mu\text{m}$ bands ($I_{12\mu\text{m}}^{\text{excess}}$, $I_{25\mu\text{m}}^{\text{excess}}$, and $I_{60\mu\text{m}}^{\text{excess}}$, respectively) relative to the total FIR emission (F_{FIR}). We find that $\Delta\nu_{12\mu\text{m}} I_{12\mu\text{m}}^{\text{excess}}/F_{\text{FIR}}$ and $\Delta\nu_{25\mu\text{m}} I_{25\mu\text{m}}^{\text{excess}}/F_{\text{FIR}}$ in the LMC are smaller than those in the Galactic plane. We conclude that smaller VSGs are less abundant in the LMC than in our Galaxy. The mid- to far-infrared SEDs in various positions in the LMC are also discussed. We find that the linearly rising branch corresponds to the data including young star clusters, while the horizontal branch corresponds to the data without young star clusters. Taking account of the contribution of multiple components with different temperatures or the distribution of the ISRF strength ranging from U_{min} to U_{max} , we can reproduce the linearly rising branch with $(U_{\text{min}}, U_{\text{max}}) = (1, 10^5)$ and the horizontal branch with $(U_{\text{min}}, U_{\text{max}}) = (0.5, 100)$. Finally, we investigate the *IRAS* $12\text{--}25\mu\text{m}$ color in CO molecular clouds, finding that the large scatter of the $12\text{--}25\mu\text{m}$ color at small $I_{12\text{CO}}$ can also be well accounted for by the contribution from molecular clouds at various locations with different U_{max} .

In the near future, photometric data sets provided by the LMC large area survey with *AKARI* covering from 2 to $170\mu\text{m}$ with

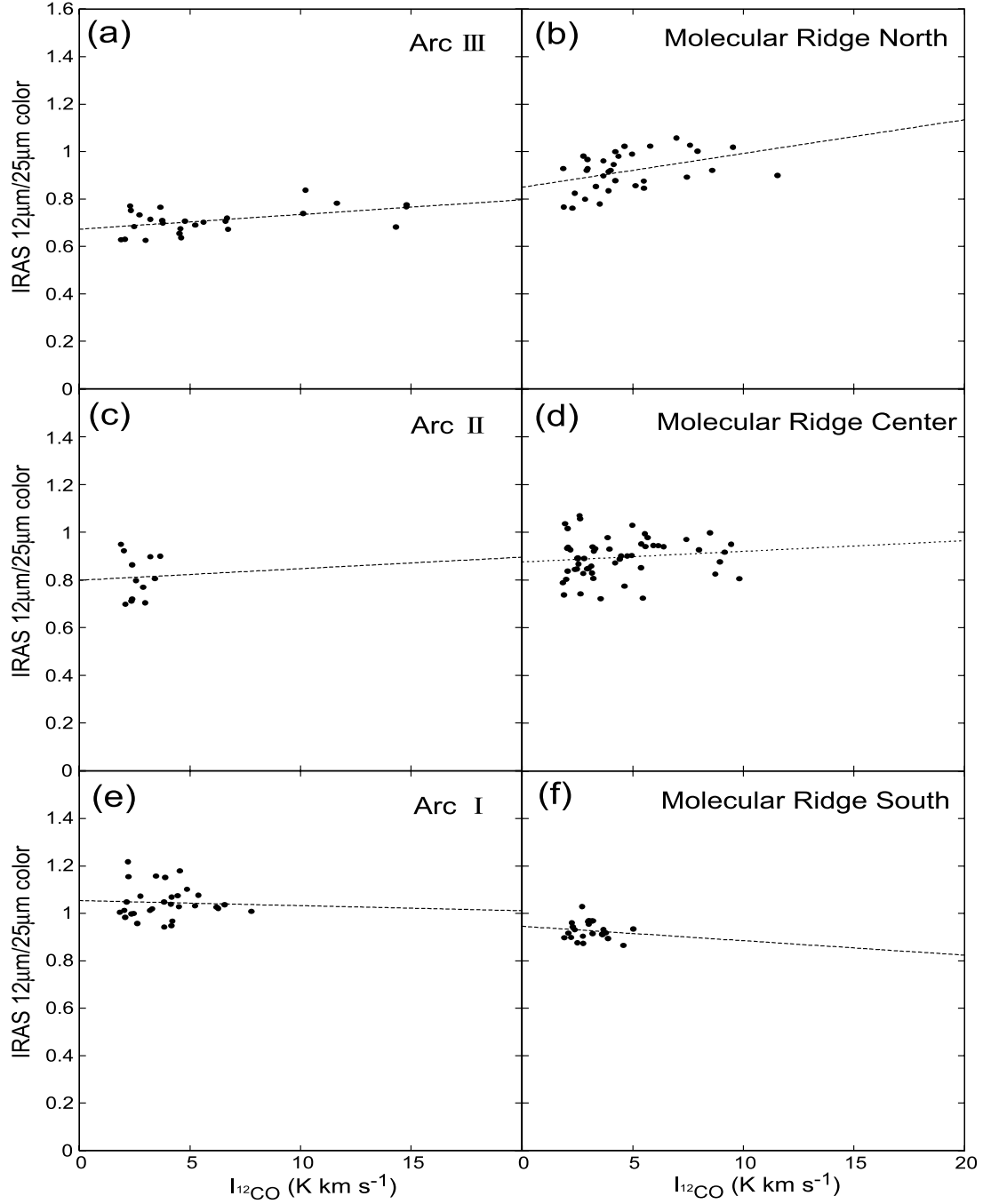


FIG. 13.—(a–f) Plots of the *IRAS* 12–25 μm color ($f_{\nu_{12 \mu\text{m}}}/f_{\nu_{25 \mu\text{m}}}$) against $I_{12\text{CO}}$ for the data that belong to arc III, molecular ridge north, arc II, molecular ridge center, arc I, and molecular ridge south, respectively. The linear fit with $f_{\nu_{12 \mu\text{m}}}/f_{\nu_{25 \mu\text{m}}} = \phi I_{12\text{CO}} + \psi$ is shown in each panel.

TABLE 4
CHARACTERISTICS OF THE MIR EMISSION IN CO MOLECULAR CLOUDS

Region	$f_{\nu_{60 \mu\text{m}}}/f_{\nu_{100 \mu\text{m}}}$	Slope (ϕ) ^a ($\text{K}^{-1} \text{ km}^{-1} \text{ s}$)	Offset (ψ) ^a
Arc III	0.399 ± 0.025	$(6.2 \pm 2.4) \times 10^{-3}$	0.67 ± 0.02
Arc II.....	0.313 ± 0.015	$(4.8 \pm 5.8) \times 10^{-3}$	0.80 ± 0.01
Arc I.....	0.214 ± 0.011	$(-2.1 \pm 8.6) \times 10^{-3}$	1.05 ± 0.04
Molecular ridge north.....	0.319 ± 0.011	$(14.2 \pm 5.7) \times 10^{-3}$	0.85 ± 0.03
Molecular ridge center.....	0.309 ± 0.012	$(4.4 \pm 5.1) \times 10^{-3}$	0.88 ± 0.03
Molecular ridge south.....	0.293 ± 0.022	$(-6.1 \pm 10.5) \times 10^{-3}$	0.95 ± 0.03

^a Parameters of the fit with $f_{\nu_{12 \mu\text{m}}}/f_{\nu_{25 \mu\text{m}}} = \phi I_{12\text{CO}} + \psi$.

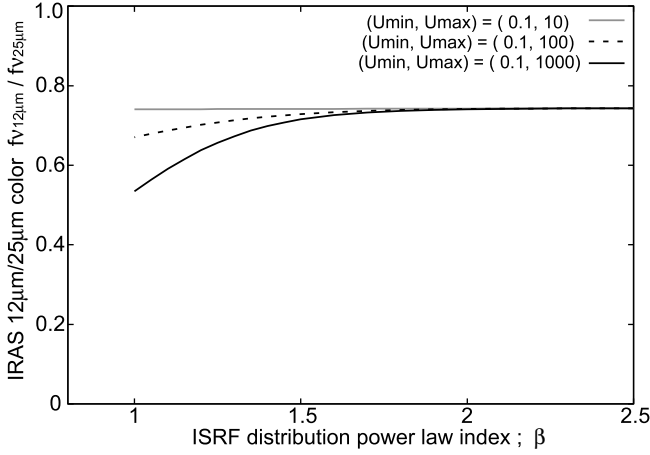


FIG. 14.— Model profiles of the *IRAS* 12–25 μm color ($f_{\nu 12 \mu\text{m}}/f_{\nu 25 \mu\text{m}}$) vs. β of eq. (5) for $(U_{\min}, U_{\max}) = (0.1, 10)$ (gray line), $(0.1, 100)$ (dashed black line), and $(0.1, 1000)$ (solid black line).

five bands in the near- to mid-infrared and four bands in the far-infrared (Matsuhara et al. 2005), as well as the products of the recent *Spitzer* survey of the Large Magellanic Cloud Surveying

the Agents of a Galaxy's Evolution (SAGE; Meixner et al. 2006) project with four Infrared Array Camera (IRAC) bands and three Multiband Imaging Photometer for *Spitzer* (MIPS) bands, will excellently resolve the individual sources on scales of less than a few parsecs, and significant progress in the understanding of the chemical evolutionary scenario of interstellar dust is expected.

The ISSA data were obtained from the NASA Astrophysics Data Center (ADC). The *COBE* data were taken from the Legacy Archive for Microwave Background Data Analysis (LAMBDA). Support for LAMBDA is provided by the NASA Office of Space Science. The LMC ^{12}CO survey data at 2.7 mm were taken by the NANTEN millimeter-wave telescope of Nagoya University. The authors are grateful to Thomas L. Roellig, Tetsuo Hasegawa, and Yasushi Nakajima for useful comments. I. S. is financially supported by the Japan Society for the Promotion of Science (JSPS). This work is supported in part by a Grant-in-Aid for Scientific Research on Priority Areas from the Ministry of Education, Culture, Sports, Science, and Technology, Japan, and from the JSPS.

APPENDIX A

SUBTRACTION PROCEDURE OF GALACTIC FOREGROUND EMISSION

We use the Parkes High-Latitude H I Survey data (Cleary et al. 1979) made with the Parkes Radio Observatory (CSIRO) to derive the Galactic foreground H I intensity. The beamwidth (HPBW) was $48'$, which is a size just comparable with the *COBE* DIRBE data sets. Since the Galactic H I emission shows a velocity distribution typically ranging from -100 to 50 km s^{-1} , we define the Galactic H I intensity $I_{\text{HI}}^{\text{Gal}}$ as

$$I_{\text{HI}}^{\text{Gal}} = \int_{-100 \text{ km s}^{-1}}^{50 \text{ km s}^{-1}} T_a(v) dv, \quad (\text{A1})$$

where T_a is the antenna temperature in each velocity channel and v is the velocity relative to the velocity of local standard of rest (VLSR).

We derive the empirical correlation between the Galactic H I line intensity ($I_{\text{HI}}^{\text{Gal}}$) and each of the *COBE* DIRBE band intensities ($I_{\nu \text{DIRBE}\lambda}^{\text{Gal}}$, where the subscript λ denotes 12, 25, 60, 100, 140, and 240 μm of the *COBE* DIRBE bands) in the off-LMC region ($90^\circ 0' < \alpha_{\text{B1950.0}} < 120^\circ 0'$, $-80^\circ 0' < \delta_{\text{B1950.0}} < -60^\circ 0'$, hereafter the reference area), where the Galactic component is dominant in each infrared band. As we can see in Figure 15, good correlations between $I_{\text{HI}}^{\text{Gal}}$ and $I_{\nu \text{DIRBE}\lambda}^{\text{Gal}}$ are found. We have made a linear fit with $I_{\nu \text{DIRBE}\lambda}^{\text{Gal}} = a_\lambda I_{\text{HI}}^{\text{Gal}} + b_\lambda$ for $I_{\text{HI}}^{\text{Gal}} < 600 \text{ (K km s}^{-1}\text{)}$, which is a typical range of $I_{\text{HI}}^{\text{Gal}}$ in the LMC region. The results of the fit are summarized in Table 5.

Figure 16a shows the 100 μm intensity map of the Galactic foreground emission in the LMC region ($I_{\nu \text{DIRBE}100 \mu\text{m}}^{\text{Gal}}$). The Galactic component distributes both in the west and in the east periphery of the LMC together with the gradual increase from the northwest (*top right*) to the southeast (*bottom left*) in each panel. This gradient is in the direction of the Galactic plane. Figure 16b shows the fraction of the Galactic foreground emission in the *COBE* DIRBE 100 μm map.

We adopt the same procedure as for the *COBE* DIRBE data set in the course of subtracting the Galactic foreground emission from the ISSA data sets. The *IRAS* was designed to detect point sources, and thus large zero-point drifts across the ISSA maps render the data unsuitable for the determination of absolute flux in regions as large as the LMC. Therefore, first we make the zero-point correction. We used the field013 image for the LMC analysis and the field014 image for obtaining the Galactic H I-to-IR relation. First we evaluated the offset of each *IRAS* band intensity of the field014 image relative to the field013 image using the data in the overlapping regions of the two fields. The estimated offsets are summarized in Table 6.

Then we derive the H I-to-IR correlation for each *IRAS* band over the off-LMC region ($95^\circ 0' < \alpha_{\text{B1950.0}} < 120^\circ 0'$, $-80^\circ 0' < \delta_{\text{B1950.0}} < -60^\circ 0'$) using the Parkes High-Latitude H I Survey data and the offset-corrected ISSA data set in field014. The results of the H I-to-IR relation for each *IRAS* band are summarized in Table 7. Although the spatial resolution of the ISSA maps is much finer than that of the Parkes maps, we assume that the variations in infrared intensity of the Galactic component in the LMC region are smooth and a simple interpolation is applied.

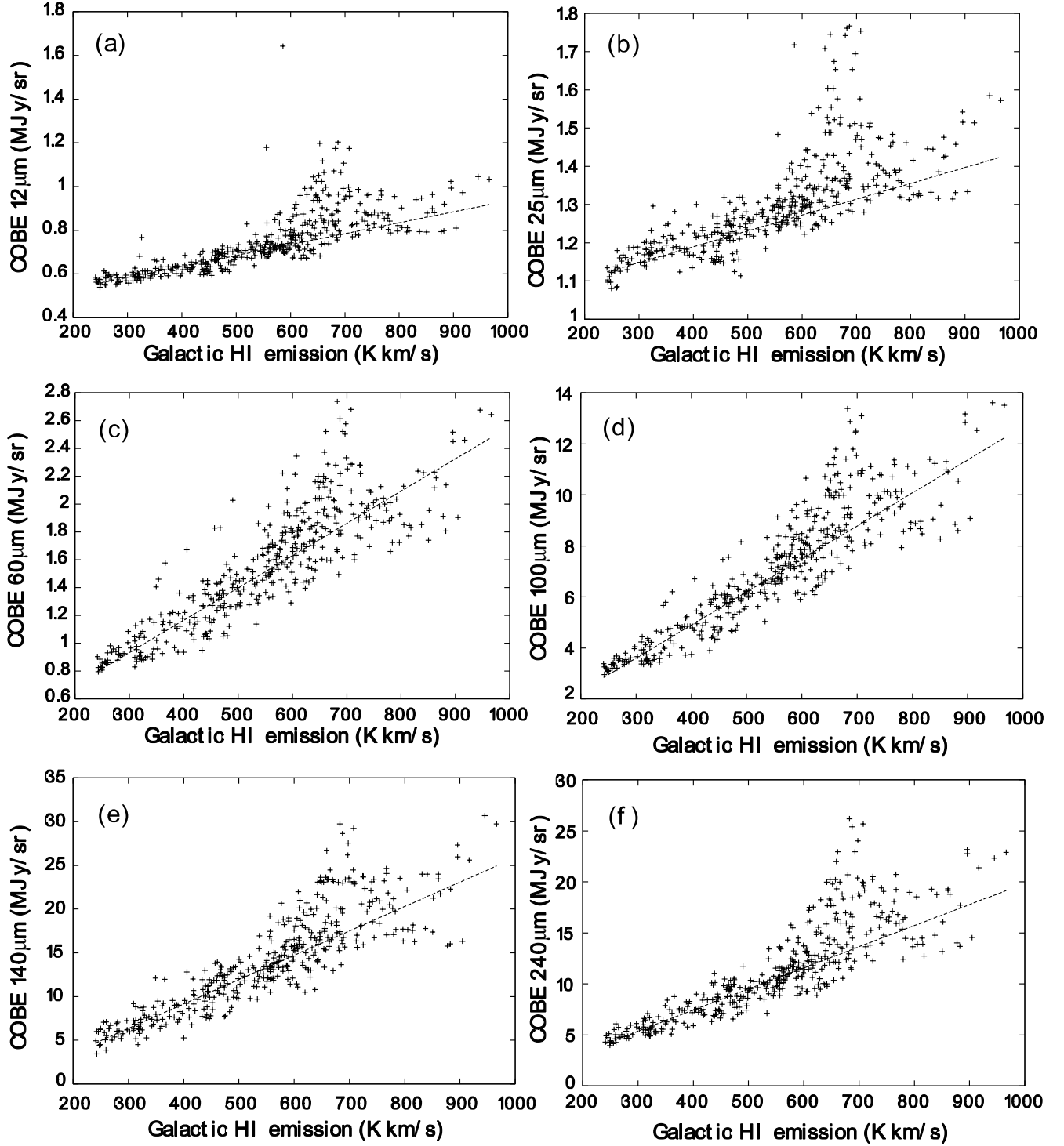


FIG. 15.—Plots of *COBE* DIRBE band intensity at (a) 12 μm , (b) 25 μm , (c) 60 μm , (d) 100 μm , (e) 140 μm , and (f) 240 μm against Galactic H I intensity in the reference area. The dotted lines in each panel shows the linear fit to the data from 200 to 600 K km s^{-1} .

APPENDIX B

LINEAR TRANSFORMATION BETWEEN THE ISSA AND THE *COBE* DIRBE ZSMA DATA

To correct the systematic difference between the ISSA and the *COBE* DIRBE ZSMA data in the LMC, we use the linear transformation with $f_{\nu_{60\mu\text{m}}}^{\text{DIRBE}} = c_{60\mu\text{m}} f_{\nu_{60\mu\text{m}}}^{\text{IRAS}} + d_{60\mu\text{m}}$ and $f_{\nu_{100\mu\text{m}}}^{\text{DIRBE}} = c_{100\mu\text{m}} f_{\nu_{100\mu\text{m}}}^{\text{IRAS}} + d_{100\mu\text{m}}$, where $f_{\nu_{60\mu\text{m}}}^{\text{IRAS}}$ and $f_{\nu_{100\mu\text{m}}}^{\text{IRAS}}$ are the foreground-subtracted flux density in megajanskys per steradian of the ISSA data, which is averaged to match with the DIRBE beam size of $21'$ in radius, $f_{\nu_{60\mu\text{m}}}^{\text{DIRBE}}$ and $f_{\nu_{100\mu\text{m}}}^{\text{DIRBE}}$ are the foreground-subtracted flux density of the ZSMA, $c_{60\mu\text{m}}$ and $c_{100\mu\text{m}}$ are the gain, and $d_{60\mu\text{m}}$ and $d_{100\mu\text{m}}$ are the offset in the transformation. Table 8 lists $c_{60\mu\text{m}}$, $c_{100\mu\text{m}}$, $d_{60\mu\text{m}}$, and $d_{100\mu\text{m}}$ with 1σ errors obtained by least-squares fits in each region.

TABLE 5
COEFFICIENTS OF THE LINEAR FIT TO THE H I-TO-IR RELATION FOR *COBE* DIRBE

<i>COBE</i> DIRBE λ Band (μm)	a_λ (MJy sr $^{-1}$ K $^{-1}$ km $^{-1}$ s)	b_λ (MJy sr $^{-1}$)	<i>COBE</i> DIRBE λ Band (μm)	a_λ (MJy sr $^{-1}$ K $^{-1}$ km $^{-1}$ s)	b_λ (MJy sr $^{-1}$)
12.....	$(5.01 \pm 0.20) \times 10^{-4}$	0.43 ± 0.01	100.....	$(1.30 \pm 0.04) \times 10^{-2}$	-0.29 ± 0.17
25.....	$(4.41 \pm 0.26) \times 10^{-4}$	1.02 ± 0.01	140.....	$(2.79 \pm 0.11) \times 10^{-2}$	-2.02 ± 0.47
60.....	$(2.32 \pm 0.08) \times 10^{-3}$	0.24 ± 0.04	240.....	$(2.07 \pm 0.07) \times 10^{-2}$	-0.84 ± 0.33

NOTE.—Coefficients of the linear transformation (see text).

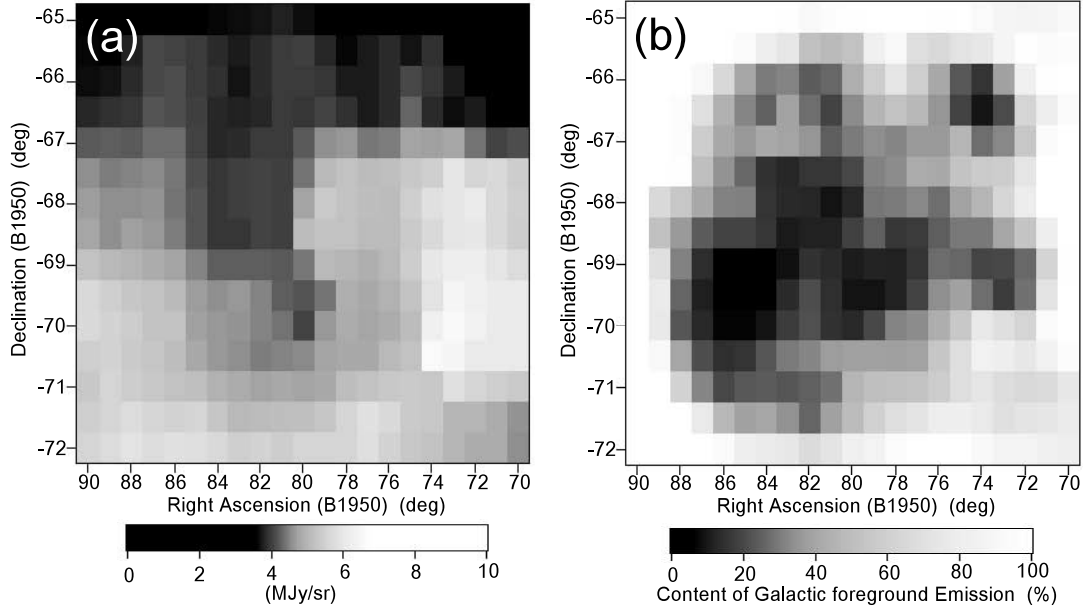


FIG. 16.—(a) Galactic foreground emission at *COBE* DIRBE 100 μm in the LMC region. (b) Fraction of Galactic foreground emission in *COBE* DIRBE 100 μm map in the LMC region.

TABLE 6
THE OFFSET OF FIELD014 RELATIVE TO FIELD013 OF THE ISSA

ISSA Band (μm)	Offset (MJy sr $^{-1}$)	ISSA Band (μm)	Offset (MJy sr $^{-1}$)
12.....	0.0201 ± 0.0003	60.....	-0.0098 ± 0.0015
25.....	-0.0240 ± 0.0005	100.....	0.0011 ± 0.0046

TABLE 7
COEFFICIENTS OF THE LINEAR FIT TO THE H I-TO-IR RELATION FOR THE ISSA DATA SETS

ISSA λ Band (μm)	a_λ (MJy sr $^{-1}$ K $^{-1}$ km $^{-1}$ s)	b_λ (MJy sr $^{-1}$)	ISSA λ Band (μm)	a_λ (MJy sr $^{-1}$ K $^{-1}$ km $^{-1}$ s)	b_λ (MJy sr $^{-1}$)
12.....	$(7.24 \pm 0.57) \times 10^{-4}$	0.64 ± 0.03	60.....	$(2.24 \pm 0.13) \times 10^{-3}$	-0.93 ± 0.07
25.....	$(5.49 \pm 0.59) \times 10^{-4}$	3.88 ± 0.03	100.....	$(1.45 \pm 0.08) \times 10^{-2}$	-1.50 ± 0.41

NOTES.—For the linear transformation of $I_{\nu\text{IRAS}\lambda}^{\text{Gal}} = a_\lambda I_{\text{H I}}^{\text{Gal}} + b_\lambda$. The subscript λ denotes 12, 25, 60, and 100 μm of the ISSA bands.

TABLE 8
LINEAR TRANSFORMATION COEFFICIENTS BETWEEN THE ISSA AND THE *COBE* DIRBE ZSMA DATA

Area	$c_{60\ \mu\text{m}}$	$d_{60\ \mu\text{m}}$ (MJy sr ⁻¹)	$c_{100\ \mu\text{m}}$	$d_{100\ \mu\text{m}}$ (MJy sr ⁻¹)
LMC.....	0.84 ± 0.01	-0.02 ± 0.09	0.82 ± 0.01	-0.01 ± 0.20
Galactic polar regions ^a	0.87 ± 0.05	0.13 ± 0.65	0.72 ± 0.07	-1.47 ± 0.88

^a From Wheelock et al. (1994).

The gain values c_λ in Table 8 are compatible with those in the ISSA-DIRBE transformation estimated for the Galactic polar regions as indicated in the last row of Table 8 (Wheelock et al. 1994).

REFERENCES

- Aguirre, J. E., et al. 2003, *ApJ*, 596, 273
Arendt, R. G., et al. 1998, *ApJ*, 508, 74
Bel, N., Viala, Y. P., & Guidi, I. 1986, *A&A*, 160, 301
Bernard, J. P., et al. 1999, *A&A*, 347, 640
Bica, E., Claria, J. J., Dottori, H., Santos, J. F. C., Jr., & Piatti, A. E. 1996, *ApJS*, 102, 57
Boudet, N., Mutschke, H., Nayral, C., Jager, C., Bernard, J.-P., Henning, T., & Meny, C. 2005, *ApJ*, 633, 272
Cartledge, S. I. B., et al. 2005, *ApJ*, 630, 355
Cleary, M. N., Heiles, C., & Haslam, C. G. T. 1979, *A&AS*, 36, 95
Dale, D. A., Helou, G., Contursi, A., Silberman, N. A., & Kolhatkar, S. 2001, *ApJ*, 549, 215
Désert, F.-X., Boulanger, F., & Pudget, J. L. 1990, *A&A*, 237, 215
d'Hendecourt, L. B., Allamandola, L. J., & Greenberg, J. M. 1985, *A&A*, 152, 130
Draine, B. T., & Anderson, N. 1985, *ApJ*, 292, 494
Finkbeiner, P. D., Davis, M., & Schlegel, J. D. 2000, *ApJ*, 544, 81
Fukui, Y. 2002, in *ASP Conf. Ser. 285, Modes of Star Formation and the Origin of Field Populations*, ed. E. K. Grebel & W. Brander (San Francisco: ASP), 24
Fukui, Y., & Sakakibara, O. 1992, *Mitsubishi Electric ADVANCE*, 60, 11
Fukui, Y., et al. 1999, *PASJ*, 51, 745
Helou, G. 1986, *ApJ*, 311, L33
Hibi, Y., Shibai, H., Kawada, M., Ootsubo, T., & Hirashita, H. 2006, *PASJ*, 58, 509
Kim, S., Staveley-Smith, L., Dopita, M. A., Freeman, K. C., Sault, R. J., Kesteven, M. J., & McConnell, D. 1998, *ApJ*, 503, 674
Kim, S., Staveley-Smith, L., Dopita, M. A., Sault, R. J., Freeman, K. C., Lee, Y., & Chu, Y.-H. 2003, *ApJS*, 148, 473
Lagache, G., Abergel, A., Boulanger, F., & Puget, J.-L. 1998, *A&A*, 333, 709
Li, A., & Draine, B. T. 2001, *ApJ*, 554, 778
———. 2002, *ApJ*, 576, 762
Mathis, J. S., Mezger, P. G., & Panagia, N. 1983, *A&A*, 128, 212
Matsuhara, H., Shibai, H., Onaka, T., & Usui, F. 2005, *Adv. Space Res.*, 36, 1091
Meaburn, J. 1980, *MNRAS*, 192, 365
Meixner, M., et al. 2006, *AJ*, in press (astro-ph/0606356)
Misselt, K. A., Clayton, G. C., & Gordon, K. D. 1999, *ApJ*, 515, 128
Miville-Deschênes, M.-A., Boulanger, F., Joncas, G., & Falgarone, E. 2002, *A&A*, 381, 209
Mizuno, N., et al. 2001, *PASJ*, 53, 971
Murakami, H. 2004, *Proc. SPIE*, 5487, 330
Nagata, H., Shibai, H., Takeuchi, T. T., & Onaka, T. 2002, *PASJ*, 54, 695
Nandy, K., Morgan, D. H., & Carnochan, D. J. 1979, *MNRAS*, 186, 421
Ogawa, H., Mizuno, A., Ishikawa, H., Fukui, Y., & Hoko, H. 1990, *Int. J. IR Millimeter Waves*, 11, 717
Onaka, T. 2000, *Adv. Space Res.*, 25, 2167
Reach, W. T., et al. 1995, *ApJ*, 451, 188
Sakon, I., Onaka, T., Ishihara, D., Ootsubo, T., Yamamura, I., Tanabe, T., & Roellig, T. L. 2004, *ApJ*, 609, 203 (erratum 625, 1062 [2005])
Sauvage, M., Vigroux, L., & Thuan, T. X. 1990, *A&A*, 237, 296
Searle, L., Wikinson, A., & Bagnuolo, W. 1980, *ApJ*, 239, 803
Shipman, R. F. 1994, *BAAS*, 26, 1355
Takagi, T., Vansevicius, V., & Arimoto, N. 2003, *PASJ*, 55, 385
Tielens, A. G. G. M., & Hagen, W. 1982, *A&A*, 114, 245
Tokura, D., Onaka, T., Sakon, I., Tajiri, Y. Y., & Takagi, T. 2005, *Proc. 9th Asian-Pacific Regional IAU Meeting*, ed. W. Sutantyo et al. (Bandung: Inst. Teknol. Bandung Press), 166
Vermeij, R., Damour, F., van der Hulst, J. M., & Baluteau, J.-P. 2002, *A&A*, 391, 1081
Weingartner, J. C., & Draine, B. T. 2001, *ApJ*, 548, 296
Werner, M. W., et al. 2004, *ApJS*, 154, 1
Wheelock, S. L., et al. 1994, *IRAS Sky Survey Atlas Explanatory Supplement* (Pasadena: JPL)
Yamaguchi, R., Mizuno, N., Onishi, T., Mizuno, A., & Fukui, Y. 2001a, *PASJ*, 53, 959
Yamaguchi, R., et al. 2001b, *PASJ*, 53, 985